

Assimilation of Dual-Polarization Radar Observations in Mixed- and Ice-Phase Regions of Convective Storms: Information Content and Forward Model Errors

DEREK J. POSSELT

University of Michigan, Ann Arbor, Michigan

XUANLI LI

University of Alabama in Huntsville, Huntsville, Alabama

SAMANTHA A. TUSHAUS

University of Michigan, Ann Arbor, Michigan, and Cooperative Institute for Meteorological Satellite Studies, Madison, Wisconsin

JOHN R. MECIKALSKI

University of Alabama in Huntsville, Huntsville, Alabama

(Manuscript received 18 October 2014, in final form 11 March 2015)

ABSTRACT

Dual-polarization Doppler radar has proven useful for the estimation of hydrometeor content and the classification of hydrometeor type. Recent studies have leveraged dual-polarization-specific information to produce improved assimilated cloud and precipitation fields from the warm rain (above freezing) portion of deep convective storms. While the strengths of dual-polarization radar observations have been conclusively shown for rain and hail hydrometeors, it is less clear how much information is provided in mixed-phase and ice-only regions.

In this paper, a Markov chain Monte Carlo (MCMC) algorithm is used to examine the information content of dual-polarization-specific variables in the ice-phase region of a convective storm. Results are used to quantify how much information is added by specific differential phase and radar correlation coefficient, as well as how this information is degraded when the assumed particle size distribution and particle density are allowed to vary. It is found that dual-polarization-specific observations (K_{dp} and ρ_{hv}) provide significant information on rimed ice content, and moderate information on pristine ice, especially where snow mass is more than 10% of the total volume hydrometeor mass. There is a significant reduction in information content for rain and a near-complete loss of information for graupel–hail and snow when the particle size distribution and ice particle densities are not well known, and there are systematic changes in radar information gain and loss with changes in hydrometeor mass. The results highlight the need for a thorough exploration of forward model sensitivities prior to performing radar data assimilation.

1. Introduction

The U.S. National Weather Service (NWS) recently completed a significant upgrade to its operational Weather Surveillance Radar-1988 Doppler (WSR-88D)

system to polarimetric (“dual-pol”) capability. Dual-pol radars transmit and receive pulses of radio frequency electromagnetic energy in both horizontally and vertically polarized directions. Differentiation between vertically and horizontally polarized signals received at the radar yields information on the shape, size, and type of hydrometeors in the observed volume (Seliga and Bringi 1976; Sachidananda and Zrnić 1987; Rinehart 1997; Straka et al. 2000; Kumjian 2013). This information has been proven to yield more accurate

Corresponding author address: Derek J. Posselt, Department of Atmospheric, Oceanic, and Space Sciences, University of Michigan, 2455 Hayward St., Ann Arbor, MI 48109-2143.
E-mail: dposselt@umich.edu

estimates of convective system rain and hail content when compared with that retrieved solely from radar reflectivity, and to show unique advantages in identifying hydrometeor type (Hall et al. 1984; Chandrasekar et al. 1990; Zrnić and Ryzhkov 1996; Ryzhkov et al. 1998; Vivekanandan et al. 1999; Carey et al. 2000; Zhang et al. 2001; Brandes et al. 2002; Bringi et al. 2003; Vivekanandan et al. 2004).

During the past 20 years, several studies have demonstrated the benefit of assimilating traditional radar reflectivity and radial velocity in convective systems, using three- or four-dimensional variational data assimilation (3DVAR or 4DVAR) methods (e.g., Sun and Crook 1997, 1998; Rabier et al. 2000; Gao et al. 2004; Sun 2005; Hu et al. 2006; Xiao et al. 2007; Kawabata et al. 2011; Schenkman et al. 2011; Wang et al. 2013; Wattrelot et al. 2014) and ensemble Kalman filter (EnKF) techniques (Caya et al. 2005; Tong and Xue 2008; Dowell and Wicker 2009; Aksoy et al. 2009; Zhang et al. 2009). The aforementioned studies also expressed the need for further improvement in radar data assimilation through more advanced assimilation schemes and strategies, more accurate observations, or both. Recent studies have begun to assess the utility of dual-pol observations for constraining convective storm structure in a data assimilation context, but this work has been hampered by the inadequate understanding of the uncertainties and noise level of dual-pol radar measurements, and the difficulty of developing radar forward operators for dual-pol variables. Early studies returned results that were mixed at best. Recently, a full polarimetric radar forward operator was developed by Jung et al. (2008a,b, 2010) and used to assimilate dual-pol variables: differential reflectivity Z_{dr} , reflectivity difference Z_{dp} , and specific differential phase K_{dp} in addition to typical radar reflectivity and radial velocity in an observing system simulation experiment (OSSE) context. These studies demonstrated significant improvement in storm initialization and short-term prediction, but also noted that the usefulness of dual-pol observations may be limited by uncertainties in the forward model and noise in the observations.

Li and Mecikalski (2010, 2012) demonstrated successful assimilation of dual-pol variables in two convective storms observed by the C-band Advanced Radar for Meteorological and Operational Research (ARMOR) using a 3DVAR framework. They demonstrated a positive impact of assimilating horizontal reflectivity Z_h , Z_{dr} , and K_{dp} observations, but noted that the improved model state did not produce forecast improvements that lasted beyond 2 h. They noted in a follow-up paper (Li and Mecikalski 2013) that differences in a radar forward model can have a

significant effect on the thermodynamic, dynamic, and microphysical structure of the storm.

The work conducted by Li and Mecikalski (2010, 2012, 2013) utilized a radar forward operator that was limited to liquid phase (warm rain) hydrometeors. Jung et al. (2010) included ice hydrometeors in their experiments, but limited their investigation to rain and hail, and used an EnKF framework to examine the sensitivity of their forward model to the assumed particle size distribution (PSD) and density. Experiments conducted to date have not yet thoroughly explored the information content of dual-pol variables in mixed-phase and ice-only regions of convective storms. The quantitative effect of uncertainty in ice density and PSD is also not clear. With this in mind, we pose the following research questions:

- 1) What are the characteristics of the information contained in forward modeled dual-pol radar data in the ice-phase portions of deep convective clouds, and how does this change with ice content and ice species present in the cloud? Do dual-pol observations contain enough information to constrain ice mass and PSD in a data assimilation context?
- 2) What role do PSD assumptions play in the estimates of dual-pol information content? Is it possible to quantify the error introduced by allowing these assumptions to vary?

In addressing these questions, our overarching science goals are to examine the information contained in dual-pol radar observations for ice-phase portions of deep convective clouds, and to support the development of a forward model for the assimilation of dual-pol information in subfreezing clouds. Perturbation studies may provide some limited information on the sensitivity of assimilation results to changes in forward model error, but have difficulty quantifying the magnitude and characteristics of that error. Data assimilation studies can yield useful information on the forecast and analysis impact of dual-pol variables, but are necessarily limited by the assumptions used in the formulation of the data assimilation schemes (e.g., linearity in the state-observation relationship and/or Gaussian error distributions). In this paper we take a Bayesian perspective, using a Markov chain Monte Carlo (MCMC; Posselt et al. 2008; Posselt and Vukicevic 2010; Posselt and Bishop 2012; Posselt et al. 2014; Posselt and Mace 2014) algorithm to sample the probability distribution of estimated rain, snow, and graupel. The form of the PDFs yields information as to whether observations have enough information to uniquely constrain hydrometeor content, and allow a computation of the information gained by the assimilation of dual-pol variables, as well as the information lost when the forward model is

allowed to have errors. We focus specifically on the gain in information provided by dual-polarization radar observables, as well as the information loss caused by variability in hydrometeor particle size distribution and ice density. Because our context is data assimilation, we perform idealized experiments using simulated radar variables as observations. This allows us to compare estimated hydrometeor content directly with a known true state, and facilitates the analysis of the role of error in the forward model. We wish to point out at the outset that the perspective we take in this study is one in which we consider only the information provided by dual-polarization radar on the local hydrometeor properties, and restrict our analysis to grid cells that have already been determined to contain cloud. While radar observations do not contribute direct knowledge of the thermodynamic state of the atmosphere, they do provide information on the presence or absence of cloud and, by extension, on whether a grid volume is saturated. In addition, successive constraint of cloud properties at multiple times will certainly have an effect on the temperature and water vapor content both within and outside of the cloud. Experiments that have performed data assimilation experiments in which with dual-polarization radar data are used at multiple times have, in fact, demonstrated the utility of dual-pol observations in this regard, particularly with respect to water vapor (e.g., [Wattrelot et al. 2014](#)).

The remainder of this paper is organized as follows. [Section 2](#) presents an overview of the WRF simulation and convective storm, the dual-polarization radar forward model, and the MCMC algorithm. Results of MCMC experiments and quantification of information content are presented in [section 3](#). A discussion of the results is offered in [section 4](#), and a summary and conclusions are presented in [section 5](#).

2. Data and methods

a. Convective storm description and WRF simulation

The Advanced Research version of the WRF Model ([Skamarock et al. 2008](#)) is used to simulate an isolated small-scale convective squall line on 23 June 2008. The storm of interest initiated as a single convective cell at approximately 1500 UTC in southern Tennessee and experienced a quick intensification in the next few hours with hail, strong winds, and lightning strikes observed along its path. The system evolved from a single cell into a linear southwest–northeast cluster of individual cells that remained relatively small in horizontal extent. Between 1900 and 2100 UTC the entirety of the system of convective elements was contained within the ARMOR domain. After 2100 UTC, the convective system continued its

movement toward the southeast, and dissipated in northwest Georgia at approximately 0100 UTC 24 June 2008.

Two 2-way interactive nested domains were used to simulate the storm, with coarse grid dimension of $450 \times 360 \times 28$ grid points, fine grid dimension of $480 \times 390 \times 28$ grid points, and horizontal grid spacings of 3 and 1 km, respectively. The model physics options include the Rapid Radiative Transfer Model (RRTM; [Mlawer et al. 1997](#)) longwave radiation, Dudhia shortwave radiation ([Dudhia 1989](#)), and Yonsei University (YSU) PBL schemes ([Hong et al. 2006](#)) in all experiments. The primary focus of the model simulation is the development stage of this storm between 1900 and 2100 UTC 23 June 2008 ([Fig. 1](#)). A more complete discussion of the simulation of this storm can be found in [Li and Mecikalski \(2012\)](#). Note that the observations presented in [Fig. 1](#) and the assimilation experiments presented in [Li and Mecikalski \(2012\)](#) used the C-band ARMOR radar and a radar forward model appropriate for C-band wavelength. We have tailored our experiments to be applicable to the operational NEXRAD network, and as such employ a wavelength of 10.7 cm in our forward model and in the forward modeled radar observables depicted in [Fig. 1](#).

b. Dual-pol forward models

1) FORWARD MODEL FRAMEWORK

The dual-polarimetric radar observational forward operator is based on the algorithm developed by [Jung et al. \(2008a,b\)](#), and designed to be consistent with the WRF single-moment 6-class (WSM6) microphysics scheme ([Hong et al. 2009](#)). Forward modeled radar variables include horizontal reflectivity (Z_h), vertical reflectivity (Z_v), radial velocity (V_r), differential reflectivity (Z_{dr}), specific differential phase (K_{dp}), and correlation coefficient (ρ_{hv}). This operator is used to calculate dual-pol radar variables from the WRF Model simulation for the information content analysis. Three types of hydrometers are considered in the radar forward operator: rain, snow, and graupel–hail. An exponential drop size distribution is assumed for each species, with fixed intercept parameter N_0 and variable slope parameter Λ . For hydrometeor species x , this is

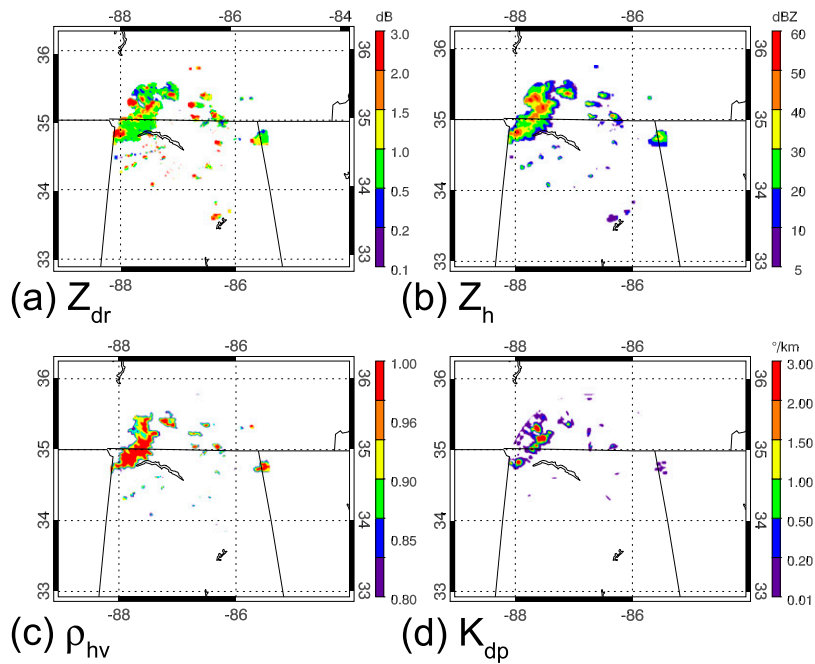
$$n(D) = N_{0,x} \exp(-\Lambda_x D), \quad (1)$$

where the slope parameter is

$$\Lambda_x = \left(\frac{\pi \rho_x N_{0,x}}{\rho_a q_x} \right)^{0.25} \quad (2)$$

with hydrometeor particle density ρ_x , mass mixing ratio q_x , and air density ρ_a . The values of the intercept

ARMOR



WRF

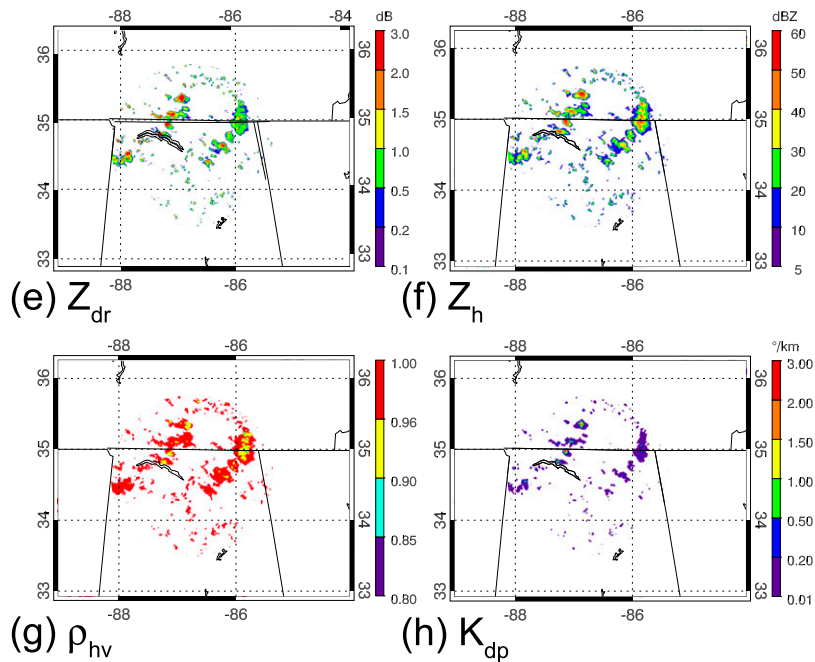


FIG. 1. Observations taken from the ARMOR radar and forward modeled observations from the WRF at 1900 UTC 23 Jun 2008, including (a),(e) differential reflectivity (dB); (b),(f) horizontal reflectivity (dBZ); (c),(g) correlation coefficient; and (d),(h) specific differential phase ($^{\circ} km^{-1}$). Both are at a height level of 2 km above the surface.

parameter for different hydrometeors are set consistent with the values found in the WSM6 scheme. For rain, snow, and graupel–hail, the intercept values are $N_{0,r} = 8.0 \times 10^6 \text{ m}^{-4}$, $N_{0,s} = 3.0 \times 10^6 \text{ m}^{-4}$, and $N_{0,g} = 4.0 \times 10^4 \text{ m}^{-4}$, respectively. The density of each species of hydrometeor is assumed to be constant and equal to 100 kg m^{-3} for snow and 500 kg m^{-3} for graupel–hail. Note that setting the hail density less than 916.7 kg m^{-3} (the value for pure ice), implicitly assumes graupel–hail is spongy and not thoroughly wetted.

Following Zhang et al. (2001) and Jung et al. (2008a,b), reflectivity on a linear scale at horizontal (Z_h) and vertical (Z_v) polarizations (in $\text{mm}^6 \text{ m}^{-3}$) can be written as

$$Z_h = \frac{4\lambda^4}{\pi^4 |K_w|^2} \int n(D) (A|f_a|^2 + B|f_b|^2 + 2C|f_a||f_b|) dD, \tag{3}$$

$$Z_v = \frac{4\lambda^4}{\pi^4 |K_w|^2} \int n(D) (B|f_a|^2 + A|f_b|^2 + 2C|f_a||f_b|) dD, \tag{4}$$

where λ is wavelength of the radar, which is 10.7 cm for NEXRAD radars. Variables A , B , and C describe the falling behavior (canting angle) of different hydrometeors; f_a and f_b are backscattering amplitudes for polarizations along the major and minor axes; and K_w is the dielectric factor of water. For rain, Z_h and Z_v (in $\text{mm}^6 \text{ m}^{-3}$) can be written as

$$Z_h = \frac{4\lambda^4 \alpha_{r,a}^2 N_{0,r}}{\pi^4 |K_w|^2} \Lambda_r^{-(2\beta_{r,a}+1)} \Gamma(2\beta_{r,a} + 1), \tag{5}$$

$$Z_v = \frac{4\lambda^4 \alpha_{r,b}^2 N_{0,r}}{\pi^4 |K_w|^2} \Lambda_r^{-(2\beta_{r,b}+1)} \Gamma(2\beta_{r,b} + 1). \tag{6}$$

For ice- and mixed-phase particles, Z_h and Z_v are

$$Z_h = \frac{\Gamma(7)\lambda^4 N_{0,x}}{\pi^4 |K_w|^2} \Lambda_x^{-7} (A\alpha_{x,a}^2 + B\alpha_{x,b}^2 + 2C\alpha_{x,a}\alpha_{x,b}), \tag{7}$$

$$Z_v = \frac{\Gamma(7)\lambda^4 N_{0,x}}{\pi^4 |K_w|^2} \Lambda_x^{-7} (B\alpha_{x,a}^2 + A\alpha_{x,b}^2 + 2C\alpha_{x,a}\alpha_{x,b}), \tag{8}$$

where $\Gamma(\dots)$ is the complete gamma function, and $\alpha_{x,a}$, $\alpha_{x,b}$ are the coefficient and index parameters describing backscattering amplitudes in the power-law form of the particle size.

Differential reflectivity in dB is computed as

$$Z_{dr} = 10 \log_{10} \left(\frac{Z_h}{Z_v} \right). \tag{9}$$

Specific differential phase is

$$K_{dp} = \frac{180\lambda N_{0,x}}{\pi} \Lambda_x^{-(\beta_{x,k}+1)} C_{k,x} \alpha_{x,k} \Gamma(\beta_{x,k} + 1). \tag{10}$$

Cross-correlation coefficient ρ_{hv} measures the correlation coefficient between the horizontal and the vertical power return:

$$\rho_{hv} = \frac{Z_{hv}}{\sqrt{Z_h Z_v}}, \tag{11}$$

where Z_{hv} is a product of two orthogonal copolar components of the radar return:

$$Z_{hv} = \frac{4\lambda^4}{\pi^4 |K_w|^2} \times \int n(D) [C(|f_a|^2 + |f_b|^2) + (A + B)|f_a||f_b|\rho_0] dD. \tag{12}$$

It can readily be seen from the forward model equations that the dual-pol variables are a function of hydrometeor mass, PSD slope intercept, and particle density.

When temperature is above 0°C , there is an option to activate a melting model used to describe hydrometeors that consist of a mixture of snow or graupel–hail and rain. It is assumed that the fraction of ice particles decreases linearly downward, while the rain fraction increases linearly upward through the melting layer. For example, the fraction of rain–snow mixture within a grid cell is defined as

$$F = F_{\max} \left[\min \left(\frac{q_s}{q_r}, \frac{q_r}{q_s} \right) \right]^{0.3}, \tag{13}$$

where $F_{\max} = 0.5$. The fraction of rain within the rain–snow mixture is

$$f_r = (Fq_r)/(Fq_s + Fq_r) = q_r/(q_r + q_s). \tag{14}$$

Density of the rain–snow mixture is parameterized as

$$\rho_m = \rho_s(1 - f_r^2) + \rho_r f_r^2. \tag{15}$$

We run the forward model without the melting parameterization by default, because the WSM6 scheme does not allow for mixed-phase hydrometeors (e.g., wet graupel or water covered snow particles). We discuss the effect of activating this parameterization later in section 4. When compared with observed dual-pol variables for the storm of interest, the forward operator generates realistic results for all of the dual-pol variables (Li and Mecikalski

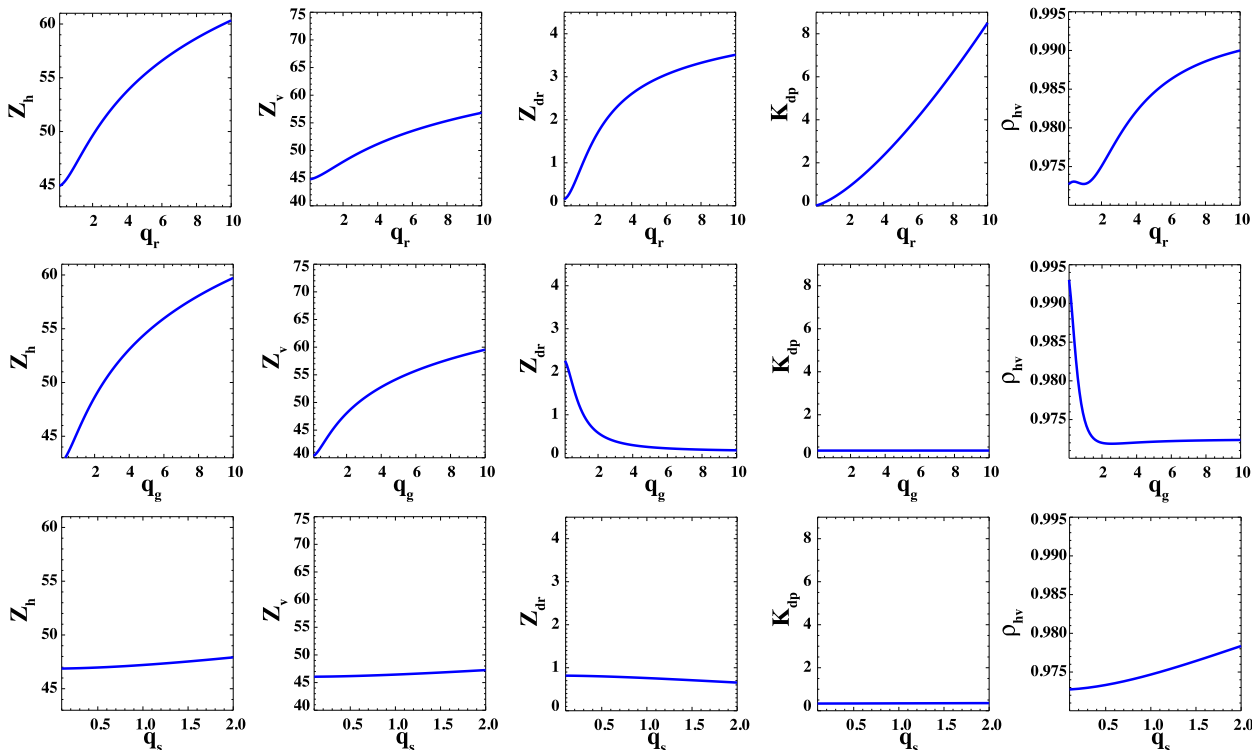


FIG. 2. Response of forward modeled (from left to right) Z_h , Z_v , Z_{dr} , K_{dp} , and ρ_{hv} to changes in (from top to bottom) rain, graupel, and snow mixing ratio (g kg^{-1}).

2012). However, the thermodynamic structure and spatial distribution of hydrometeors in the model is quite different from those observed in the storm.

2) SENSITIVITY OF FORWARD MODELED DUAL-POLARIZATION RADAR OBSERVATIONS TO CHANGES IN ICE MASS, ICE DENSITY, AND PARTICLE SIZE DISTRIBUTION

Prior to conducting a Bayesian analysis of the dual-pol radar variables, we first examine the sensitivity of forward modeled dual-pol radar variables to changes in ice mass (Fig. 2) and PSD and density (Fig. 3) using a response function analysis. We vary one state variable at a time across a specified range of values, holding all others constant (Table 1). The specific values used in these experiments correspond to the mixed-phase WRF grid point used in our MCMC experiments in section 3. Note that we use graupel as our variable of choice as this is the form taken by heavily rimed ice in the WSM6 scheme. In reality, there is not a clear distinction between graupel and spongy hail in models, the difference (for a given size) being largely a function of the amount of liquid water and solid (air free) ice in the hydrometeor. Indeed, the rimed ice category in many single-moment microphysical schemes is readily converted from graupel to hail by changing the assumed particle density and size

distribution. As such, in essence we are emulating the transition from graupel to hail by varying the graupel density from low (dry spongy graupel) to high (wet graupel–hail) and allowing the PSD intercept to vary from low (more large particles) to high (more small particles). Since the WSM6 does not allow for the coexistence of liquid and ice in the graupel–hail category, we do not treat melting by default in our experiments. Sensitivity to implementation of a melting parameterization is explored later in the discussion.

The results demonstrate a strong sensitivity of all dual-pol forward observations to changes in rain hydrometeor content (Fig. 2). As we shall see, this has implications for regions of the cloud where rain is present, as well as regions where it is not. In contrast, there is very little sensitivity to changes in snow mass mixing ratio. This is unsurprising given 1) the wavelength of the radar is large compared to the typical snow particle size, and 2) the density of snow particles is, by default, assumed to be low (100 kg m^{-3}). Note that if we had set the default snow density higher, consistent with either riming or a change in the habit assumption, changes in snow mixing ratio and PSD intercept would have had a larger influence on the radar signal. Changes in graupel mass have an effect similar in magnitude on the forward observations as changes in rain, with the

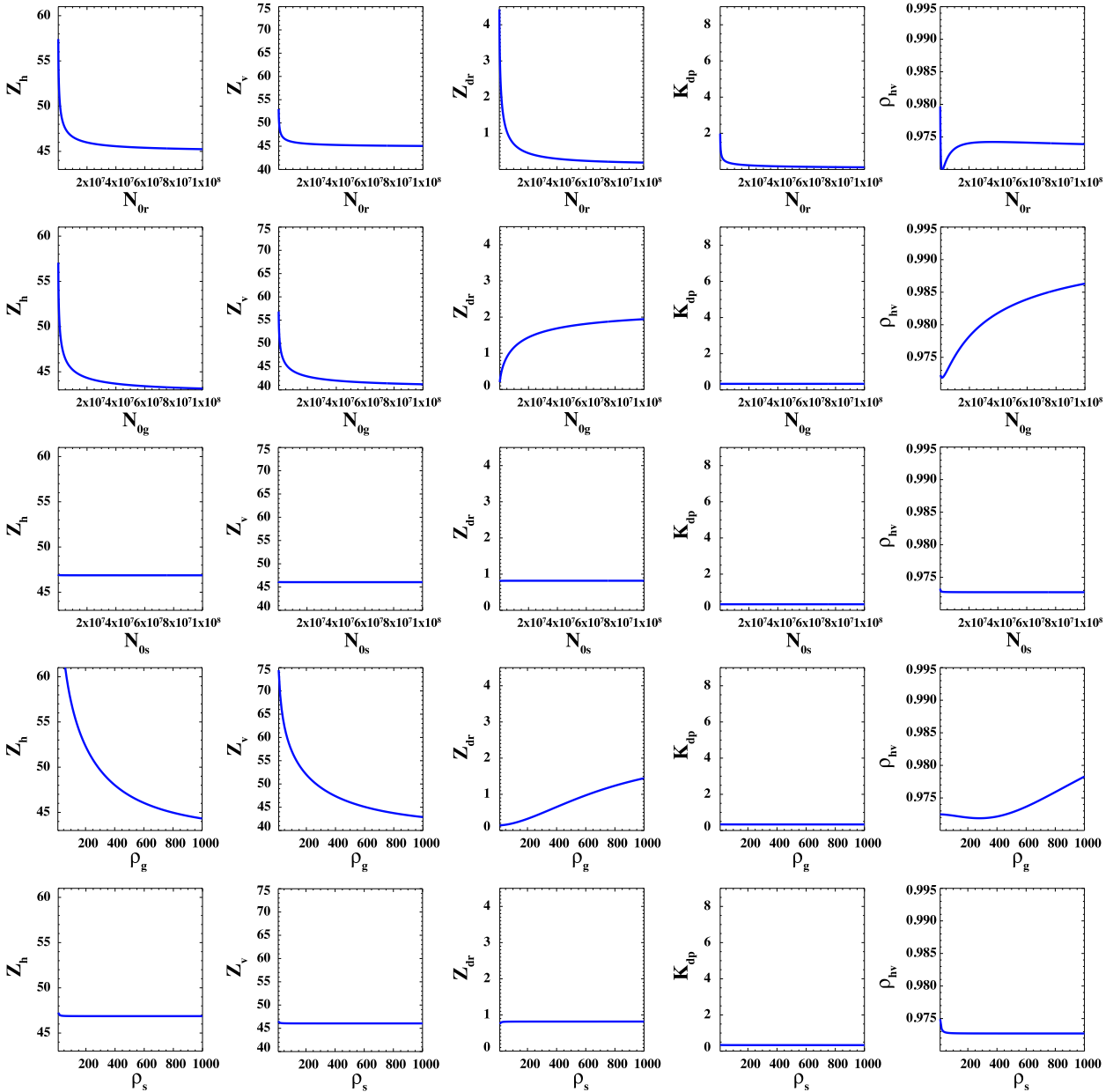


FIG. 3. As in Fig. 2, but for changes in PSD intercept (m^{-4}) for rain ($N_{0,r}$), graupel ($N_{0,g}$), and snow ($N_{0,s}$); and density (kg m^{-3}) of graupel and snow.

exception of K_{dp} , which is known to be relatively insensitive to changes in ice content. Note also that the sensitivity to Z_{dr} decreases with an increase in graupel mass as particles become more spherical with increasing mass, in contrast to rain, which becomes increasingly nonspherical with increasing mass. The ρ_{hv} measures the uniformity in the scanned volume, and large values (close to 1.0) of ρ_{hv} indicate the homogenous particle type. As such, once there is a sufficient hydrometeor content, a change in the graupel or hail mass has little effect on ρ_{hv} . This is only true if the particles do not

contain both liquid and ice; the results are quite different for mixed-phased particles.

As with the mixing ratios, the PSD intercept parameter and density of snow (Fig. 3) have a negligible influence on the forward modeled radar observables. Radar observations are sensitive to changes in the intercept of the rain and graupel number concentrations, but note that the sign of the response is the inverse of that seen in the mixing ratio responses (Fig. 2). This is due to the fact that, for a given mass, an increase in the slope intercept of the PSD implies a larger number of

TABLE 1. List of cloud state variables and forward model parameters, along with their ranges and values used in mixed-phase and ice-only experiments. See text for definition of variables.

Parameter	Units	Min	Max	Mixed phase	Ice only
q_r	g kg^{-1}	0.0	10.0	1.004	0.0
q_s	g kg^{-1}	0.0	10.0	0.107	0.714
q_g	g kg^{-1}	0.0	10.0	1.436	0.670
$N_{0,r}$	m^{-4}	1.0×10^5	1.0×10^8	8.0×10^6	8.0×10^6
$N_{0,s}$	m^{-4}	1.0×10^5	1.0×10^8	3.0×10^6	3.0×10^6
$N_{0,g}$	m^{-4}	1.0×10^5	1.0×10^8	4.0×10^6	4.0×10^6
ρ_s	g m^{-3}	1.0	1000.0	100.0	100.0
ρ_g	g m^{-3}	1.0	1000.0	500.0	500.0
T	K	—	—	273.25	261.71
P	hPa	—	—	644.72	494.97
q_v	g kg^{-1}	—	—	5.97	3.22
ρ_a	kg m^{-3}	—	—	0.819	0.658

small particles, consequently decreasing reflectivity and decreasing (increasing) asymmetry for rain (graupel). This highlights the well-known nonuniqueness problem in radar observations: for single-frequency radar, large numbers of small particles appear very similar to a few large particles. The strong sensitivity in the radar reflectivity to changes in the graupel density arises from the fact that the PSD slope parameter Λ is proportional to the particle density. The slope parameter is in turn inversely proportional to the horizontal and vertical reflectivity. As such, when the density (and, hence, the slope) increases, the radar reflectivity decreases.

The response function results indicate that, if particle number and density are fixed, dual-pol radar observations should place a strong constraint on the mass of rain and graupel (as, indeed, has been demonstrated in numerous studies). It does not appear that dual-pol radar should place a constraint on the snow mass. The responses of the forward model to changes in rain and graupel number and density indicate that, should these be allowed to vary, a not insignificant amount of uncertainty will be introduced into the estimate. It is this uncertainty that we aim to address in the following sections.

c. MCMC algorithm and Bayesian perspective on observation uncertainty

1) BAYESIAN PERSPECTIVE ON OBSERVATION UNCERTAINTY

Data assimilation produces an estimate of a set of geophysical quantities by combining prior information on the state of the system with a set of measurements. This information is quantified by assigning each source a probability distribution, and the estimate is computed as the solution to Bayes's relationship for conditional probabilities:

$$P(\mathbf{x} | \mathbf{y}) = \frac{P(\mathbf{y} | \mathbf{x})P(\mathbf{x})}{P(\mathbf{y})}, \quad (16)$$

where \mathbf{x} is the set of estimated quantities and \mathbf{y} are the observations; $P(\mathbf{x})$ represents prior knowledge of \mathbf{x} , while $P(\mathbf{y})$ is a normalizing factor that integrates over the probability space containing all possible observations. The probability of obtaining the observations \mathbf{y} from a given set of parameter values \mathbf{x} is quantified via the likelihood $P(\mathbf{y} | \mathbf{x})$. The optimal estimate of \mathbf{x} is defined as the maximum likelihood (most probable) point in the posterior conditional PDF $P(\mathbf{x} | \mathbf{y})$. Uncertainty in the estimate can be quantified via calculation of the width of the posterior PDF [e.g., posterior (co)variance, interquartile range, etc.].

It is clear from Eq. (16) that the relationship between \mathbf{x} and \mathbf{y} , as stated in the likelihood function $P(\mathbf{y} | \mathbf{x})$, is a key contributor to the estimate. Because the measurements are rarely also the geophysical quantities themselves, a model (or set of models) is required that maps from geophysical parameter space to observation space. Even if the analyzed and observed variables are the same, interpolation in space and time is commonly required. The *forward problem* describes the generation of simulated observations from a set of geophysical variables or control parameters. The likelihood is meant to represent the probabilistic relationship between \mathbf{x} and \mathbf{y} . As such, it should include an estimate of the measurement uncertainty, and also account for the functional form of the forward model that maps from values of \mathbf{x} to corresponding values of \mathbf{y} . Any uncertainty in this forward relationship should be incorporated into the likelihood function. This means that, in reality, the likelihood is made up of two components: one due to the uncertainty in the measurements, and the other due to the uncertainty in the relationship between \mathbf{x} and \mathbf{y} . It is reasonable to assume that the forward model errors

and instrument errors are independent of one another, and as such we may compute the likelihood as

$$P(\mathbf{y} | \mathbf{x}) = P(\mathbf{y} | \mathbf{x}_{\text{true}})P(f(\mathbf{x}) | \mathbf{x}). \quad (17)$$

Here, $P(\mathbf{y} | \mathbf{x}_{\text{true}})$ represents the measurement error: the error the observation would have if measuring the true state. Term $P(f(\mathbf{x}) | \mathbf{x})$ represents the probability of producing the correct forward observations $\mathbf{y} = f(\mathbf{x})$ from a given state \mathbf{x} . Clearly, if the forward model is exact, then the likelihood reduces to the measurement error. What is interesting is the fact that there may still be errors in a perfect observation if there is uncertainty in the forward operator.

Consider two experiments: one in which there is no error in the forward model and one in which uncertainty in the forward model is allowed. Further assume that the measurement error distribution is identical in each case. We would like to assess the increase in error associated with uncertainty in the forward model, expressed as a difference in some measure over the respective probability distributions $P(f_1(\mathbf{x}) | \mathbf{x})$ and $P(f_2(\mathbf{x}) | \mathbf{x})$, where f_1 and f_2 represent different levels of assumed forward model uncertainty. If the prior estimate $P(\mathbf{x})$ does not change, and the space containing all possible solutions $P(\mathbf{y})$ also does not change, then this measure can be computed from the posterior probability distributions $P(\mathbf{x} | \mathbf{y}, f_1(\mathbf{x}))$ and $P(\mathbf{x} | \mathbf{y}, f_2(\mathbf{x}))$. As such, a single computation of the Bayesian posterior distribution provides information on the solution space and the characteristics of the forward model error. In the next section, we describe a method by which an estimate of $P(\mathbf{x} | \mathbf{y})$ can be obtained that preserves the properties of $f(\mathbf{x})$ (nonlinearity, etc.), and does not restrict the probability distributions to any particular form.

2) MCMC ALGORITHM

Markov chain Monte Carlo methods provide a solution to Eq. (16) that does not require assumptions as to the specific form of the probability distributions (e.g., Gaussian, as is the case in variational data assimilation and ensemble Kalman filters), and utilizes the full nonlinear forward model. MCMC algorithms sample the posterior probability distribution via a random walk that consists of multiple sequential runs of the forward model. In each iteration, candidate values of all control parameters are randomly drawn from a *proposal distribution* centered on the current parameter estimate. The forward model is then used to produce simulated observations from the candidate parameter values and the resulting forward observations and prior are compared with the observations via a likelihood function $P(\mathbf{y} | \mathbf{x})$. The proposed set of parameter values $\hat{\mathbf{x}}$ (and the corresponding set of forward modeled observations $\hat{\mathbf{y}}$) are

accepted as a sample of the posterior probability distribution with probability:

$$Q(\mathbf{x}_i, \hat{\mathbf{x}}) = \min[1, \rho(\mathbf{x}_i, \hat{\mathbf{x}})], \quad (18)$$

where \mathbf{x}_i is the previously accepted parameter set and the acceptance ratio $\rho(\mathbf{x}_i, \hat{\mathbf{x}})$ is defined as

$$\rho(\mathbf{x}_i, \hat{\mathbf{x}}) = \frac{P(\hat{\mathbf{y}} | \hat{\mathbf{x}})P(\hat{\mathbf{x}})q(\hat{\mathbf{x}}, \mathbf{x}_i)}{P(\mathbf{y}_i | \mathbf{x}_i)P(\mathbf{x}_i)q(\mathbf{x}_i, \hat{\mathbf{x}})}. \quad (19)$$

Here, $q(\hat{\mathbf{x}}, \mathbf{x}_i)$ is the *proposal distribution*, and represents the probability of randomly transitioning from the current parameter set \mathbf{x}_i to the proposed parameter set $\hat{\mathbf{x}}$. Conversely, $q(\mathbf{x}_i, \hat{\mathbf{x}})$ represents the probability of randomly transitioning from the proposed parameter set $\hat{\mathbf{x}}$ back to the current parameter set \mathbf{x}_i . If the proposal distribution is symmetric, $q(\mathbf{x}_i, \hat{\mathbf{x}}) = q(\hat{\mathbf{x}}, \mathbf{x}_i)$, and Eq. (19) simplifies to the ratio of prior and likelihoods. Our implementation of the MCMC algorithm uses an uncorrelated Gaussian proposal distribution centered on the current set of parameter values, with a variance that is adaptively tuned during an initial set of forward model calculations (Haario et al. 1999; Tamminen and Kyrola 2001; Posselt 2013) to strike a balance between fine-grained sampling of local probability maxima and gradients (small variance) and efficient sampling of all possible values of \mathbf{x} (large variance). Parameter sets generated during the proposal variance tuning process are not included in the posterior solution.

Note that the form of likelihood and prior in MCMC are completely general—any distribution shape may be assumed. The value of the acceptance ratio $\rho(\mathbf{x}_i, \hat{\mathbf{x}})$ determines whether the proposed set of parameters is stored as a sample of the posterior distribution. If the new set of parameters produces an improved fit to the observations, then this set is saved as the next sample in the distribution. If not, then a test value is drawn from a uniform distribution. If this value is less than the acceptance ratio, the proposed parameter values are saved; if not, the proposed set of parameters is rejected, the current set is stored as another sample, and new proposed parameter values are drawn. The accept-reject procedure is central to the operation of an MCMC algorithm, and ensures that randomly chosen parameter sets with higher probability (better fit to the observations) are automatically accepted, while parameter values that provide a similar (but perhaps poorer) fit to observations are considered. Parameter sets that produce simulated observations far from the measurements are rejected. In the process, the algorithm preferentially samples high-probability regions of the posterior parameter space, avoids very low

TABLE 2. Dual-polarization radar observables, their forward computed values for each case, and their observation uncertainties.

Observation	Units	Mixed phase	Ice only	Error σ
Z_h	$\text{mm}^6 \text{m}^{-3}$	46.89	38.46	2.0
Z_v	$\text{mm}^6 \text{m}^{-3}$	46.07	38.33	2.0
Z_{dr}	$\text{mm}^6 \text{m}^{-3}$	0.820	0.134	0.5
K_{dp}	$^\circ \text{km}^{-1}$	0.336	0.006	0.5
ρ_{hv}	None	0.973	0.978	0.01

probability regions, and appropriately samples the parameter space in between. The probabilistic accept–reject procedure allows the algorithm to move away from local probability maxima, and is the primary reason MCMC is not simply an optimization algorithm. Considered as a whole, the sequence of randomly generated parameter vectors accepted as samples of the posterior distribution is the Markov chain. At the user’s discretion, an MCMC algorithm can be constructed so that it uses a single Markov chain, or multiple chains simultaneously exploring the probability distribution associated with the same set of observations (Posselt 2013). For the sake of parallelizing the algorithm over many grid points, we use single chains in this study.

The sample of the posterior PDF generated by an MCMC algorithm represents the most complete characterization of the solution for a given forward model, prior, and set of measurements. It allows identification of sources of uncertainty, quantification of observation information content, and straightforward testing of the impact of changes to observation uncertainty and the introduction of new observations. The implementation of the MCMC algorithm in this paper is based on the algorithm described in Posselt et al. (2008) and Posselt and Mace (2014, hereafter PM14). As in PM14, the prior probability density function for all control variables is assumed to be uniform with minimum and maximum bounds set to physically realistic values of each of the hydrometeor mixing ratios, PSD parameters, and densities (Table 1). Ranges of hydrometeor mass are set intentionally large to allow the algorithm the freedom to explore multiple possible combinations of mass, PSD, and density, and PSD intercept values are consistent with observed liquid and ice particle size distributions (Tokay and Short 1996; Roy et al. 2005; Heymsfield et al. 2002). As with the hydrometeor mass mixing ratios, particle densities are also allowed a broad range with the intent of sampling widely in the parameter space. The observation likelihood is assumed to adhere to a Gaussian distribution, consistent with current operational practice, and the assumed error

TABLE 3. List of parameters varied and the number of MCMC iterations used in each experiment.

Variable parameters	No. of MCMC iterations
q_r, q_s, q_g	5×10^4
$q_r, q_s, q_g, N_{0,r}, N_{0,s}, N_{0,g}$	5×10^5
$q_r, q_s, q_g, N_{0,r}, N_{0,s}, N_{0,g}, \rho_s, \rho_h$	1×10^6

standard deviations and forward modeled values for the two grid points considered in the first set of experiments are reported in Table 2. Several MCMC experiments are performed, with the intent of assessing the increase in uncertainty in the estimated hydrometeor contents associated with variability in the PSD intercepts and densities. Increasing the number of degrees of freedom necessarily requires an increase in the number of MCMC iterations. Analysis of a multivariate Gaussian distribution (Haario et al. 1999) indicates approximately 10 000 (20 000) iterations should be sufficient to sample a 3- (8) dimensional parameter space. To allow for non-Gaussianity in the posterior distribution, we run 50 000, 500 000, and 1 000 000 iterations for 3-, 6-, and 8-dimensional PDFs, respectively (Table 3).

3. Results

a. Bayesian analysis of the utility of DPR for ice-phase cloud characterization

We now use MCMC to explore the extent to which dual-polarization radar observations are capable of estimating ice content, and assess the effect that variability in particle size distribution parameters and ice densities has on dual-pol observation information content.

The fundamental questions we seek to answer are the following:

- 1) If particle size distribution intercept values and ice particle densities are specified, can dual-polarization radar observations be used to effectively constrain grid point cloud variables? What is the nature of the solution space?
- 2) If we relax the assumption that the PSD properties and ice densities are known, what is the effect on the information content of dual-pol radar?

We begin by assuming the ice densities and higher moments of the particle size distribution are known. We consider two grid points: one containing a mixture of rain, snow, and graupel, and another containing only snow and graupel, and determine whether assimilation of dual-pol observations will result in effective constraint of

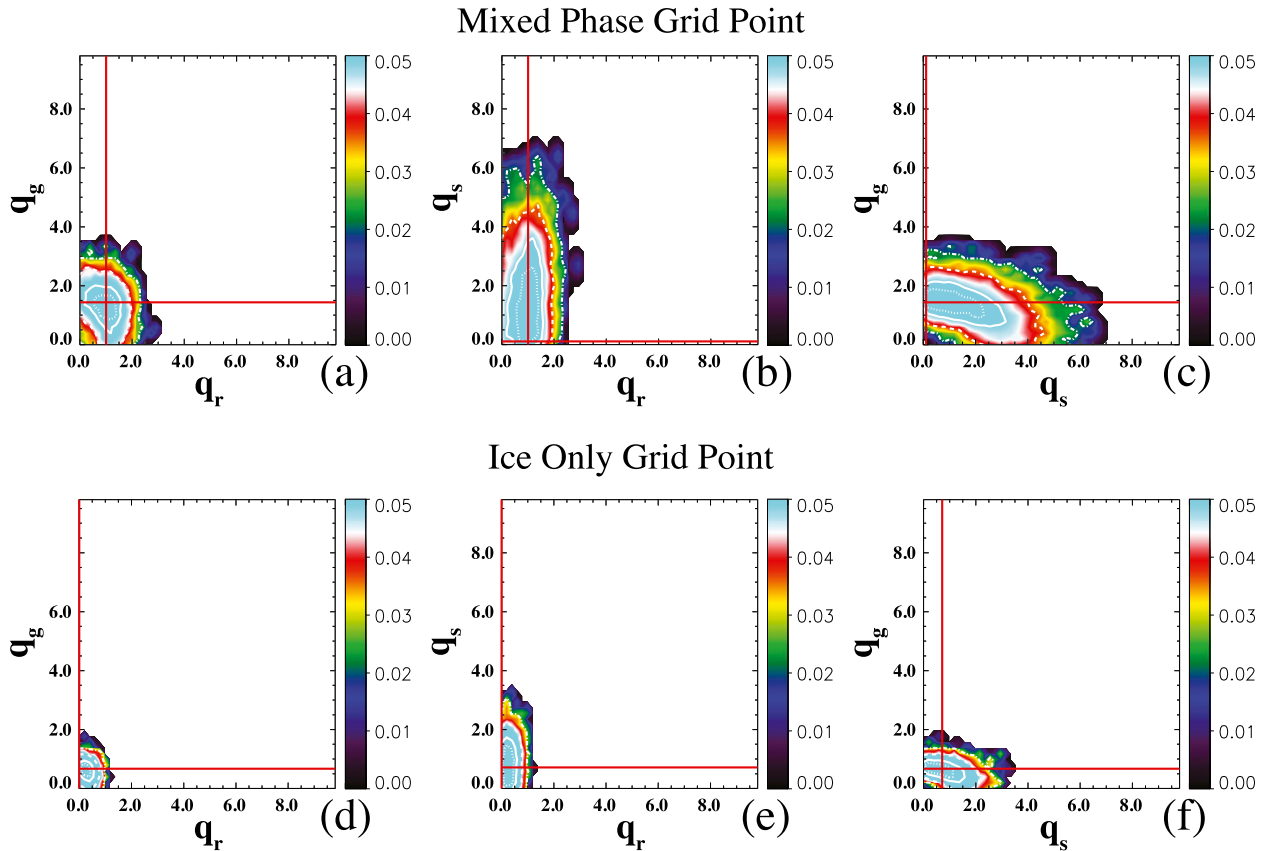


FIG. 4. The 2D marginal PDFs (color shading) for (a),(d) rain and graupel; (b),(e) rain and snow; and (c),(f) snow and graupel mixing ratios (g kg^{-1}) for (a)–(c) mixed-phase and (d)–(f) ice-only grid points. True values of each mixing ratio are depicted in the red vertical and horizontal lines, and the white contours correspond to 99.7% (dash-dot), 95% (dashed), 68.3% (solid), and 37.5% (dotted) probability.

hydrometeor mass mixing ratios. The chosen grid points each have relatively large cloud condensate amount (Table 1); experiments with relatively small amounts of condensate produced qualitatively similar results, and are not presented here. Three separate MCMC experiments are performed: the default assumes only Z_h , Z_v , and Z_{dr} are available as observations, while subsequent experiments add information from observations of K_{dp} and ρ_{hv} .

Figure 4 depicts two-dimensional marginal PDFs from the MCMC-generated Bayesian posterior distribution $P(\mathbf{x} | \mathbf{y})$ for the case in which only mixing ratios are allowed to vary and dual-pol radar reflectivity observations are used as constraints in the MCMC algorithm. Figures 4a–c correspond to the mixed-phase grid point, while the PDFs in Figs. 4d–f were obtained for the ice-only grid point. We will explore the changes in the marginal distributions associated with assimilation of different dual-pol observations and variability in PSD and density momentarily. Analysis of these figures primarily serves to provide an indication of the shape of the posterior solution space. A number of conclusions

may be drawn (keeping in mind that this analysis is performed for only two grid points). First, rain and graupel mass are well constrained by radar reflectivity: a single maximum likelihood point is evident in Figs. 4a and 4d. Second, while snow mass is not well constrained at low values of snow mass mixing ratio (probability is nearly uniform over a range between 0 and 2 g kg^{-1}), the algorithm precludes large snow mass, indicating the radar observations place an upper bound on the snow content in the volume. Third, the uniform probability of snow mass between 0.0 and 4.0 g kg^{-1} for the mixed-phase grid point (Fig. 4b) and between 0.0 and 2.0 g kg^{-1} for the ice-only grid point is in fact covariability with graupel (Figs. 4c and 4f). Large snow mass and small graupel mass produce the same radar forward observations as large graupel mass and small snow mass. Finally, while the PDFs are symmetric in the immediate region of the maximum likelihood point, they are by nature hard bounded at zero. This immediately introduces skewness into the solution as the PDF is truncated on one side and unbounded on the other. It has been shown (Posselt et al. 2014) that

the assumption that hard-bounded variables are Gaussian in nature can lead to significant problems in ensemble-based assimilation algorithms. An evaluation of the effect of Gaussian assumptions on the assimilation of dual-pol radar variables is not the topic of this study, but we mention it here to caution users that these issues are potentially a problem for any assimilation exercise that assumes a Gaussian PDF for variables that are naturally bounded.

It is notable that the PDFs in the ice-only case have identical shape to those in the mixed-phase case. The only difference is that the rain mixing ratio is constrained to far smaller values for the grid point in which rain is absent. This highlights the utility of dual-pol observations in regions of the atmosphere that support rain, but for which rain is absent; dual-pol radar is an excellent rain detector.

The WSM6 single-moment microphysical scheme used in WRF assumes the particle number density is known. We now relax this assumption and examine the effect on the posterior marginal distributions. Figure 5 depicts the marginal probability densities for rain, snow, and graupel obtained from several experiments. Each row corresponds to a different cloud hydrometeor species, while each column corresponds to different measures of variability in the PSD and particle densities. In the first column, PSD parameters and ice density are assumed fixed, while the slope intercept parameters are allowed to vary in the experiments shown in the middle column. The intercepts and ice densities are all allowed to vary in the experiments represented in the column at right. In each plot, 1D marginal distributions are shown for cases in which only reflectivity is observed (blue), reflectivity and K_{dp} are observed (black), and reflectivity, K_{dp} , and ρ_{hv} are observed (red). As such, transition from left to right represents increasing uncertainty in the forward model, while progression from blue to black to red represents increasing observational constraint.

The first column essentially confirms, in a 1D context, what was shown in Fig. 4: rain and graupel mass (Figs. 5a and 5d) are well constrained when any combination of dual-pol observations are used, but note that addition of ρ_{hv} (red) places a strong constraint on the graupel mass. Snow is very poorly constrained in general (Fig. 5g), though it is notable that the addition of ρ_{hv} has a positive effect on the estimate of the snow mass. This is likely due to the fact that the graupel is well constrained by the correlation coefficient. Since the posterior distribution of snow covaries with graupel (Figs. 4c and 4f), improved constraint on graupel leads to improved constraint on snow as well.

The sensitivity of the forward model to changes in particle number has a clearly discernible effect on the solution when PSD parameters are allowed to vary. There is a near complete loss in uniqueness of the solution for all variables. Rain is still relatively well constrained (Fig. 5b), especially when all dual-pol variables are used as observations, but there is a significant increase in the posterior variance for graupel and snow (Figs. 5e and 5h). In fact, there is near-zero information on the snow content (the posterior PDF is uniform) when reflectivity and K_{dp} are assimilated, with small constraint offered by the correlation coefficient (Fig. 5h).

In the experiments described above, it was assumed that the density of snow and graupel–hail is perfectly known. If we relax this assumption, we introduce additional uncertainty into the estimate. When ice densities are allowed to vary, the posterior PDF of the rain mass changes little (Fig. 5c), but there is a nearly complete loss of information on the graupel and snow mass (Figs. 5f and 5i). Assimilation of K_{dp} and ρ_{hv} has little effect on the distributions. Now, consider a grid point that contains only ice (snow and graupel; Tables 1 and 2). When there is no rain in the grid box, there is much improved constraint on the snow and graupel mass, especially when the ice densities are held constant (left and middle columns, Fig. 6). Constraint on the graupel mass remains when ice densities are allowed to vary (Fig. 6f), but now the snow mass is completely unconstrained (Fig. 6i). Note that, while the most likely state is one in which there is no rain present, there is still significant probability of obtaining a result with some rain, with mass mixing ratios as large as 1 g kg^{-1} in the perfect forward model, and 2 g kg^{-1} when PSD and ice densities are allowed to vary.

Additional insight into the conditional relationships between variables can be seen in plots of the joint parameter distributions. Visualization of a marginal joint distribution in more than two dimensions is difficult, but insight into the structure in the (in this case) 8-dimensional PDF can be obtained by examining 2D marginal distributions for each pair of variables. Figures 7 and 8 depict all two-dimensional marginal distributions for the mixed-phase and ice-only grid points, respectively. Comparison of the two figures reveals that the structure of the solution for mixed-phase and ice-only grid points is quite similar. This is a key point, as it illustrates the fact that the underlying functional relationships between changes in input variables and changes in forward observations determine the character of the solution space. What is also clear is the fact that the width (dispersion) of the

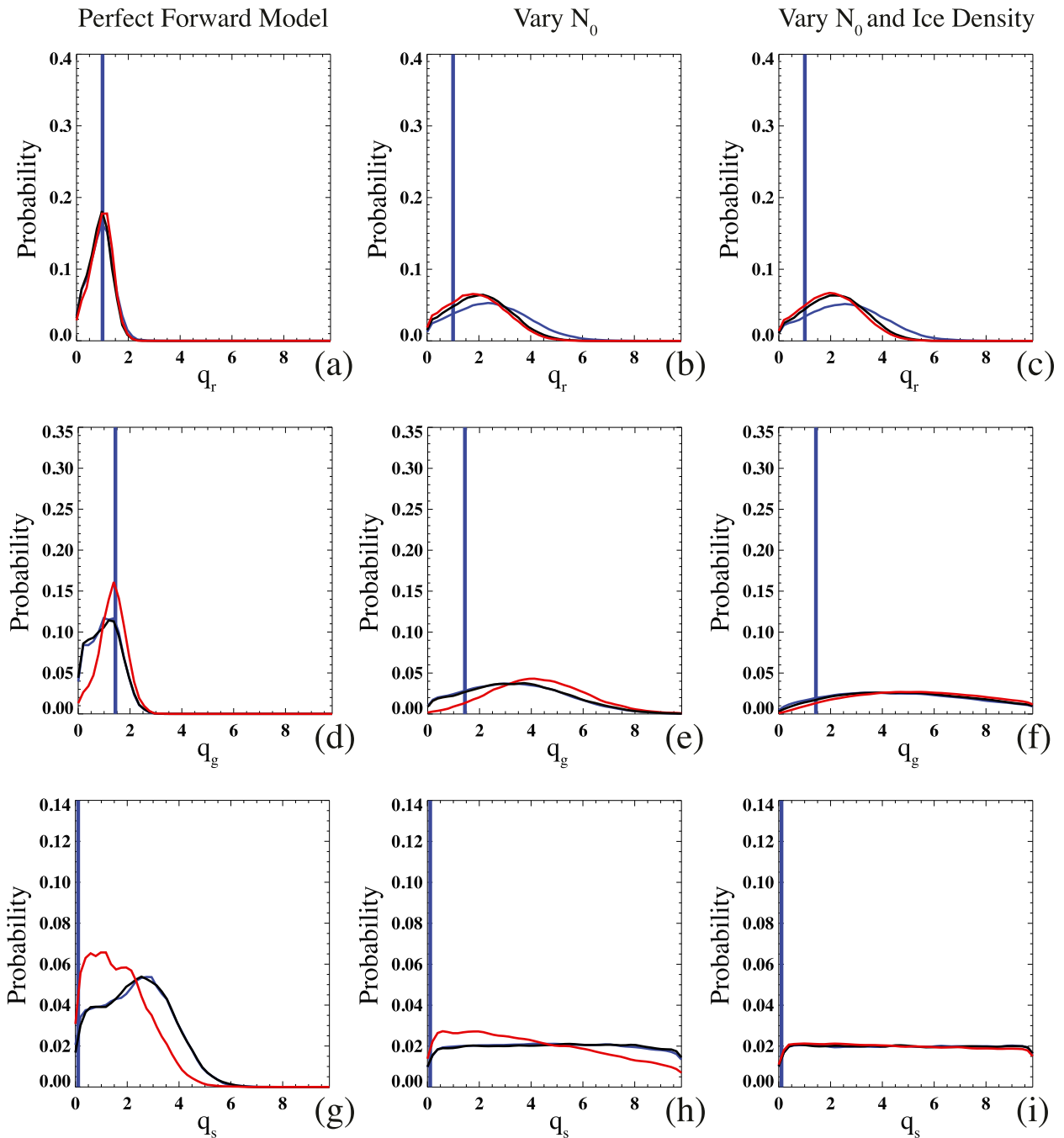


FIG. 5. The 1D marginal probability distributions for (a)–(c) rain, (d)–(f) graupel, and (g)–(i) snow mixing ratios (g kg^{-1}) as a function of variables assimilated and for increasing variability in the forward model. Experiments depicted in (a),(d),(g) assume particle size distribution intercept and ice particle density are known. Experiment results in (b),(e),(h) assume ice density is known, but size distribution intercept is not; and results in (c),(f),(i) assume that PSD intercept and ice density are unknown. Observations used in each experiment are reflectivity (Z_h , Z_v , and Z_d ; blue lines), reflectivity + specific differential phase (Z_h , Z_v , and Z_{dr} , and K_{dp} ; black lines), and reflectivity + specific differential phase + correlation coefficient (Z_h , Z_v , and Z_{dr} , and K_{dp} and ρ_{hv} ; red lines). Blue vertical lines depict the true mixing ratio value in each case.

posterior error distributions is a function of the water mass in the grid box; larger water content is associated with larger probability dispersion (a measure of uncertainty in the estimate). It is worth noting that

data assimilation and retrieval methods predicated on the assumption that the posterior PDF can be constructed via linear perturbation analysis have difficulty reproducing this behavior unless the

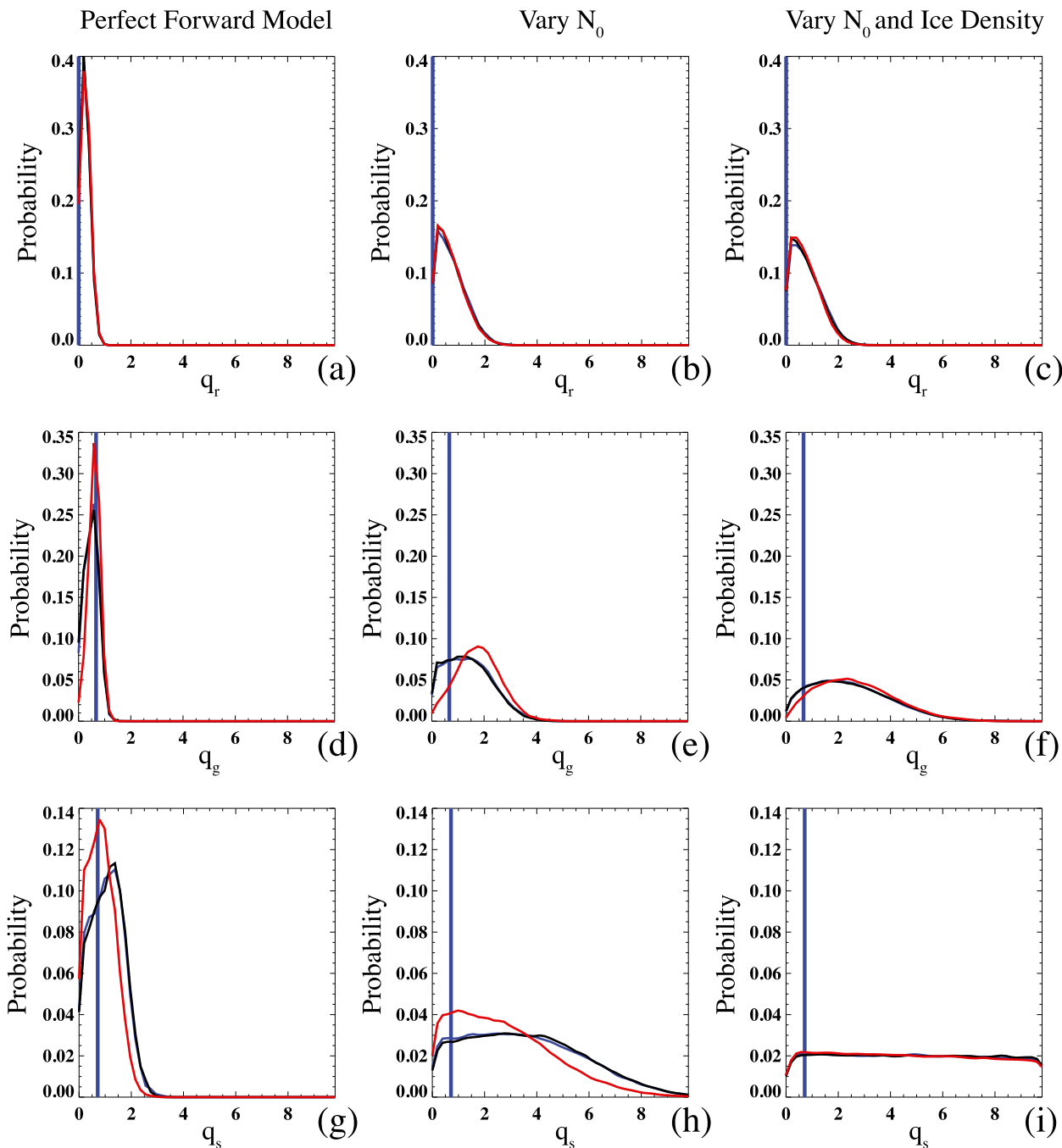


FIG. 6. As in Fig. 5, but for the ice-only grid point.

observation error is made an explicit function of the observation magnitude.

Clear covariability can be seen in the joint marginal distributions of q_r and $N_{0,r}$, q_g and $N_{0,g}$, and q_g and ρ_g in each plot. Each of these makes physical sense: to produce the same set of forward radar observations, as mass increases, the slope intercept of the PSD must also increase so that there are larger numbers of small

particles and, hence, the same forward modeled radar reflectivity. Graupel mass and density covary because of the formulation of the particle size distribution: mass is in the numerator and density in the denominator of the PSD slope parameter Λ . In addition, there is clear constraint on the rain mass in the mixed-phase grid point and on the rain and graupel in the ice-only grid point. Finally, the reason for the apparent

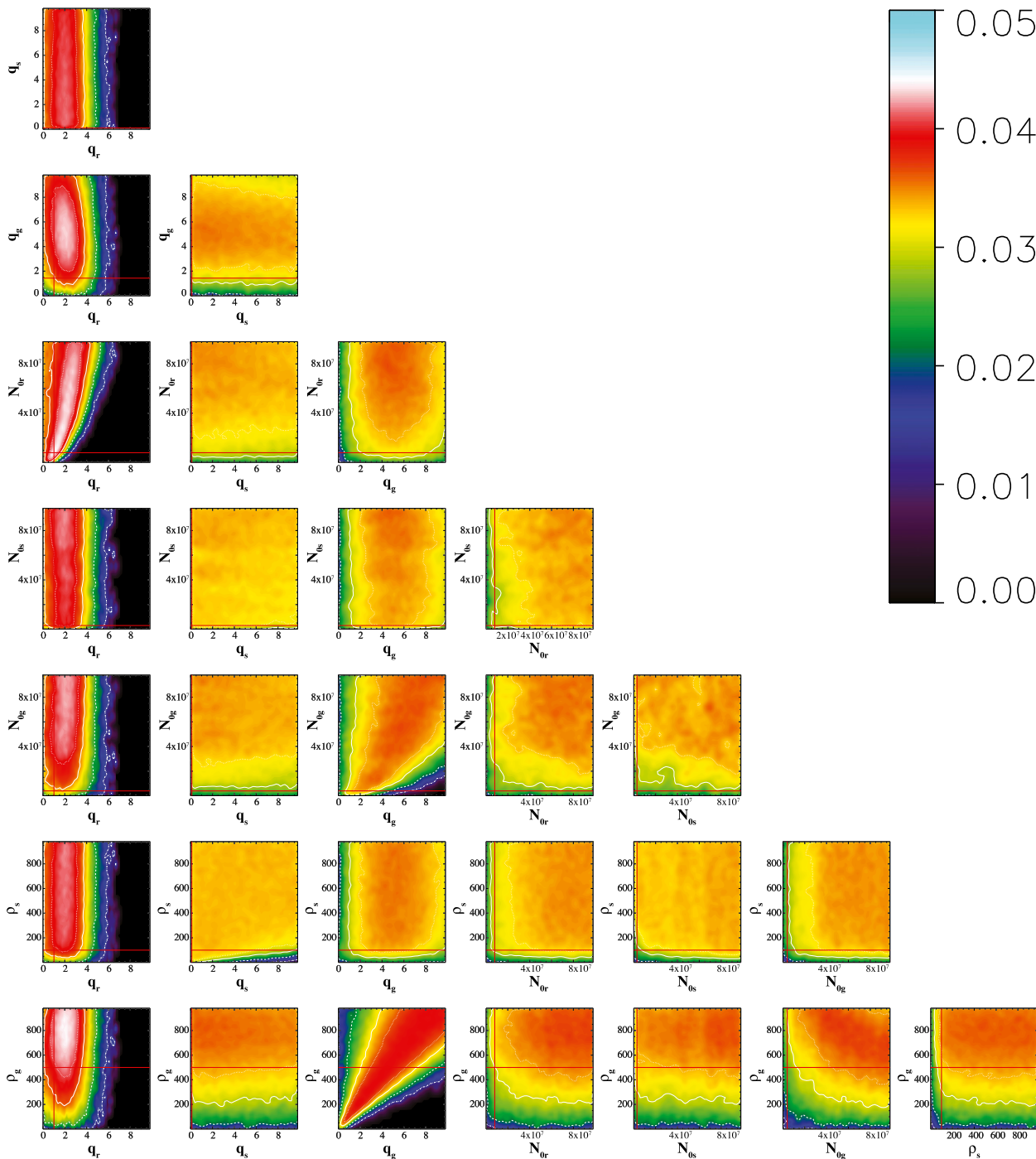


FIG. 7. All 2D marginals for the mixed-phase grid point for the case in which all observations are used in the assimilation and all dual-pol forward model parameters are allowed to vary: (first column) q_r vs (top to bottom) q_s , q_g , N_{0r} , N_{0s} , N_{0g} , ρ_s , and ρ_g ; (from the second column to the last column) as in first column, but for q_s , q_g , N_{0r} , N_{0s} , N_{0g} , ρ_s , and ρ_g , respectively, vs remaining quantities. Color-filled and line contours are as in Fig. 4.

shift in mode away from the true graupel mass becomes apparent when the PDFs are viewed in 2D. Because of the covariability of the graupel mass and graupel density and number, much of the mass of the

PDF lies at values far from the truth. When the eight-dimensional PDF is integrated over seven dimensions, the covariability makes the 1D marginal PDF appear to have a mode that is located at values far from the true value.

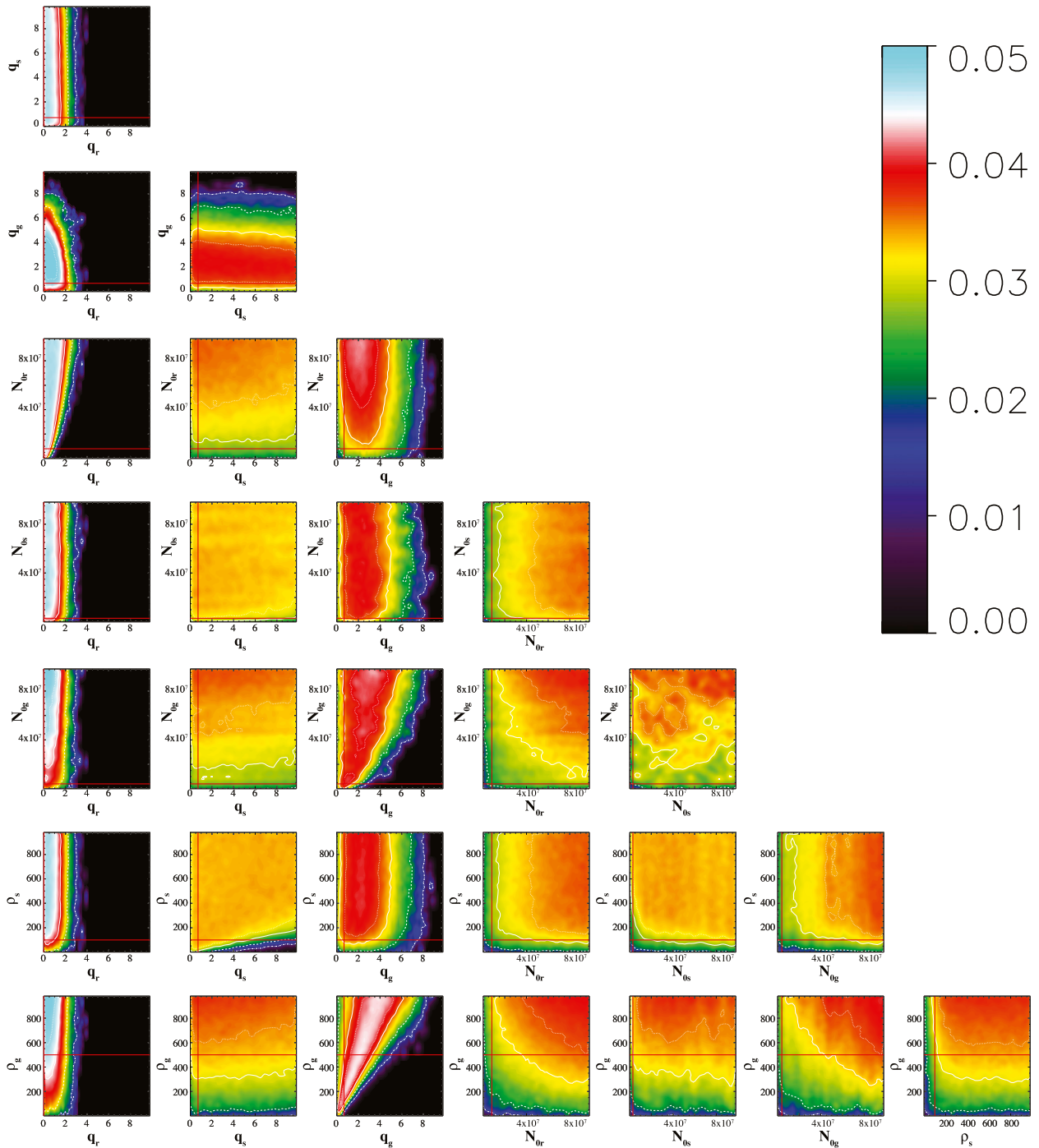


FIG. 8. As in Fig. 7, but for the ice-only grid point.

b. Information content analysis

1) INDIVIDUAL GRID POINTS

It is clear from the preceding analysis that assimilation of dual-pol variables adds value to the analysis, especially when PSD parameters and ice densities are

assumed known. Even when they are not, dual-pol observations still result in a constraint on rain mass and, to a lesser extent, graupel. In this section we quantify the information gain associated with assimilation of the dual-pol variables, as well as the information loss when PSD parameters and ice densities

TABLE 4. Information gain (columns 1–2) and loss (columns 3–4) with addition of observation information and with increased variability in forward model parameters. Columns 5–7 depict the fractional inflation on the assumed observation error due to forward model errors. Boldface text indicates where information content results are robust to changes in probability bin size.

	$H(K_{dp})$	$H(\rho_{hv})$	$-H(N_{0,x})$	$-H(\rho_x)$	% Inflation ($N_{0,x}$)	% Inflation (ρ_x)	% Inflation (total)
Rain	0.058	0.006	-0.624	-0.003	154.1	100.2	154.4
Snow	0.002	0.146	-0.572	-0.030	148.7	102.1	151.9
Graupel	-0.011	0.063	-0.846	-0.161	179.7	111.8	200.9

are allowed to vary. From a theoretical perspective, information can be quantified by considering the entropy of a given state. Given a probability distribution P , the entropy $S(P)$ can be written for the discrete case as (Rodgers 2000)

$$S(P) = -\sum_{i=1}^N p_i \log_2(p_i), \quad (20)$$

where p_i is the probability mass in discrete interval i . The information provided by a set of observations can be quantified by examining the difference between the entropy of the state before and after the addition of the observations. One commonly used measure is the Shannon information content $H = S(P_1) - S(P_2)$ (Rodgers 2000), where the entropy is computed in log base 2 so that H is represented in bits of information. Note that in our case P_1 and P_2 are two posterior conditional probability distributions, and may be computed using two different sets of observations or two different sets of forward model uncertainty assumptions. In the former case, H quantifies the information gain between case 1 and case 2, while in the latter H measures the information loss due to increased forward model uncertainty.

Now, if the probability distributions P_1 and P_2 are Gaussian, the computation of H reduces to

$$H = S(P_1) - S(P_2) = \frac{1}{2 \ln 2} \ln |\Sigma_1 \Sigma_2^{-1}|, \quad (21)$$

where Σ_1 is the covariance associated with probability distribution P_1 and Σ_2 the covariance associated with probability distribution P_2 . Note that the factor of $\ln 2$ in the denominator has the effect of expressing the information content in units of bits. We see in Eq. (21) a natural expression of the ratio of posterior

covariances. Since the ratio of posteriors is directly related to the ratio of likelihoods if the priors are the same, computation of the information content H allows an estimate of the factor by which observation uncertainty must be inflated to account for forward model error. Rearranging Eq. (21), if Σ_2 is the posterior covariance obtained from a constrained (assumed error free) forward model, and Σ_1 is the posterior covariance obtained using a forward model with errors, the error variance inflation factor due to forward model error is

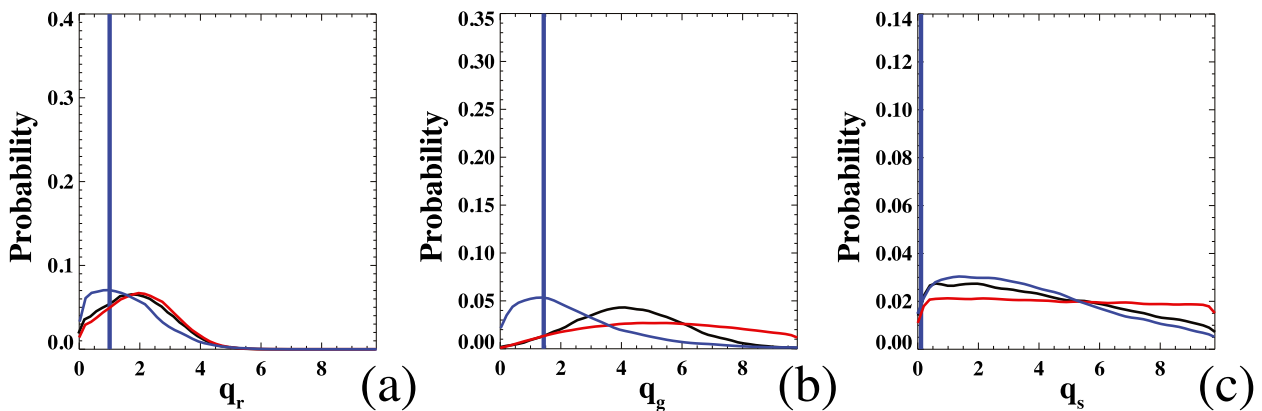
$$\Sigma_1 \Sigma_2^{-1} = \exp[2 \ln 2 (H)]. \quad (22)$$

Results of the information content analysis are presented in Tables 4 and 5 for the mixed-phase and ice-only grid points, respectively. Note that information content less than 0.1 bits is deemed not to be robust, as it is sensitive to changes in the discrete PDF bin size. Information in Tables 4 and 5 that is robust to changes in bin size is indicated in boldface text. The first four columns of each table contain the information in bits computed according to Eq. (20) gained by addition of observations of K_{dp} and ρ_{hv} , and lost via variability in PSD intercept and particle density. The last three columns contain the percent inflation on an assumed Gaussian observation error standard deviation [computed from Eq. (22)] due to variability in PSD intercept, particle density, or both. Examination of the results for the mixed-phase grid point reveals there is little information gain from the addition of K_{dp} observations (first column, Table 4) for all of the hydrometeor types. In essence, if only the hydrometeor contents are allowed to vary, rain and graupel are well constrained by radar reflectivity; and the addition of K_{dp} does not help to improve the estimate of snow. Note that the very small negative values of K_{dp} information

TABLE 5. As in Table 4, but for the ice-only grid point.

	$H(K_{dp})$	$H(\rho_{hv})$	$-H(N_{0,x})$	$-H(\rho_x)$	% Inflation ($N_{0,x}$)	% Inflation (ρ_x)	% Inflation (total)
Rain	0.012	-0.011	-0.644	-0.026	156.3	101.8	159.1
Snow	0.002	0.113	-0.847	-0.245	179.9	118.5	213.2
Graupel	-0.009	0.108	-0.880	-0.364	184.1	128.7	236.8

Mixed Phase Grid Point



Ice Only Grid Point

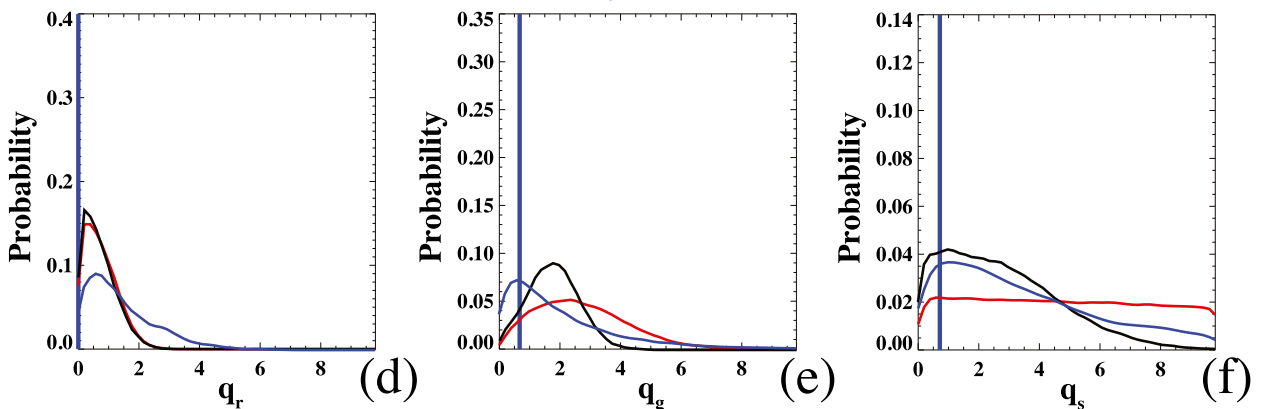


FIG. 9. The 1D marginal distributions for (a),(d) rain; (b),(e) graupel; and (c),(f) snow mixing ratio for the (a)–(c) mixed-phase grid point and the (d)–(f) ice-only grid point. PDFs are depicted for cases in which mixing ratios and PSD intercepts vary (black); all parameters including PSD intercept and ice density vary (red); and only mixing ratios vary but error in the observations is inflated (blue).

in the graupel content case in both Tables 4 and 5 are an artifact of the discrete PDF binning and should be considered to be zero information. Addition of ρ_{hv} observations improves the estimate of snow content, but does not change the (already well constrained) rain and graupel content.

Variability in the PSD intercept results in a significant loss in information. In fact, far more information is lost because of variability in the PSD than is gained via assimilation of K_{dp} and ρ_{hv} . The losses are worst for graupel content, but rain and snow are strongly affected as well. When particle densities are allowed to vary, rain and snow are not affected, but there is a loss in information for graupel. In total, the losses in information result in error inflation factors of approximately 150% for rain and snow, and approximately 200% for graupel. Similar results are obtained for the

ice-only grid point, though in this case variability in particle density results in a more significant loss in information for snow and graupel than in the mixed-phase case. Consequently, while the error inflation factor for rain remains close to 150%, the inflation factors for snow and graupel are now 213% and 236%, respectively.

We test whether observation error inflation can account for the variability in PSD and particle densities by running an additional MCMC experiment for each grid point in which variability is only allowed in the hydrometeor mass (PSD and ice densities are fixed), but the observation errors are inflated by 200% for the mixed-phase and ice-only grid points, respectively. These numbers represent the approximate mean of the total inflation factors for each grid point. Marginal PDFs from each experiment are depicted in Fig. 9.

TABLE 6. List of parameters varied and the number of MCMC iterations per grid cell used in whole-domain experiments.

Variable parameters	Observations	No. of MCMC iterations
q_r, q_s, q_g	Z_h, Z_v, Z_{dr}	1×10^4
q_r, q_s, q_g	Z_h, Z_v, Z_{dr}, K_{dp}	1×10^4
q_r, q_s, q_g	$Z_h, Z_v, Z_{dr}, K_{dp}, \rho_{hv}$	1×10^4
$q_r, q_s, q_g, N_{0,r}, N_{0,s}, N_{0,g}$	$Z_h, Z_v, Z_{dr}, K_{dp}, \rho_{hv}$	5×10^4
$q_r, q_s, q_g, N_{0,r}, N_{0,s}, N_{0,g}, \rho_s, \rho_g$	$Z_h, Z_v, Z_{dr}, K_{dp}, \rho_{hv}$	1×10^5

Examination of the PDFs of rain (first column) indicates inflation is largely successful at capturing the increased error variance, though the variance is somewhat overestimated for the ice-only grid point. Inflation causes snow PDFs to closely approximate those that result from PSD parameter variability, but is not able to represent the loss of information associated with variability in particle density. Inflation does not result in the correct approximation for the graupel PDF in either case—while the overall variance is increased, the posterior PDF still exhibits a mode near the true value, while the true posterior PDFs have a mode nearer the center of the range. The fact that error inflation does not produce PDFs that are identical to the true posterior PDFs is primarily due to the fact that the inflation factor is based on the assumption of a Gaussian PDF, while posterior distributions are clearly non-Gaussian for most variables. The bottom line conclusion from the information content analysis is that variability in the PSD parameters and particle densities results in up to 560% inflation in the observation uncertainty.

2) WHOLE-STORM INFORMATION CONTENT

While a detailed analysis of select grid points provides insight into many aspects of the radar information content, it is by nature limited. A more complete analysis should necessarily consider a large range of cloudy grid points. To this end, we conduct an MCMC-based analysis of a portion of the WRF domain that corresponds approximately to the ARMOR radar range. Following Fig. 1, this corresponds to a region that spans approximately 87.5° to 86.5°W longitude and 34.5° to 35.5°N latitude. This portion of the model domain contains a total of 324 000 grid points. Of these, 2.8% (9173 grid points) contain at least 0.01 g kg⁻¹ of either snow or graupel. Of these, 4742 are mixed phase (contain >1 × 10⁻³ g kg⁻¹ rain) and 4431 are rain free. We run 5 MCMC experiments for each of the 9173 ice-containing or mixed-phase grid points in the ARMOR domain (Table 6). These are, as in the single gridpoint results reported in section 3b(1), designed to highlight the information gained by addition of K_{dp} and ρ_{hv} when mixing ratios are the

only variables, then to quantify the loss of information when number concentrations and particle densities are allowed to vary.

Information content and error inflation factor are depicted in the first and second rows of Fig. 10, respectively. As in the single gridpoint analysis, we examine the information gained by adding observations of K_{dp} and ρ_{hv} when only the mixing ratios are allowed to vary, and the information loss when particle size distribution and ice particle densities are assumed to be unknown. As in the single gridpoint case (Tables 4 and 5), observations of K_{dp} add little information to the estimate of graupel (Fig. 10b) or snow (Fig. 10c). Analysis of several thousand grid points with differing water content now allows us to see that the information gain from K_{dp} increases as a function of rainwater content (Fig. 10a). There is no additional information gained by assimilation of ρ_{hv} for rain, and the slight gain in information for graupel and snow is independent of hydrometeor content (Figs. 10b,c). As in the single gridpoint results, the information loss associated with variability in PSD intercept and ice particle density is far greater than the information gain associated with assimilation of K_{dp} and ρ_{hv} . Allowing variability in ice density inflates error significantly, but only for ice content, and predominantly at low ice content values [$<2 \text{ g kg}^{-1}$ graupel (Figs. 10b,e), and $<0.2 \text{ g kg}^{-1}$ snow (Figs. 10c, f)]. In contrast, variability in the PSD intercept leads to significant loss of information for all hydrometeors, but especially for graupel and snow. Error increases with increasing rain content, while it decreases with increasing snow and graupel content. This is due to the fact that rain content is well constrained by dual-pol observations at nearly all values of the rain mixing ratio. By contrast, as ice content increases, information in the observations saturates (around a value of 2 g kg^{-1} graupel and 0.1 g kg^{-1} snow). Above these values, there is little additional information in the observations. The loss of information is greater at large rain mixing ratio values because there is more information to lose. Note that the observation error inflation estimates are state dependent; they are a strong function of the mixing ratio. Note also that they are far higher in general for

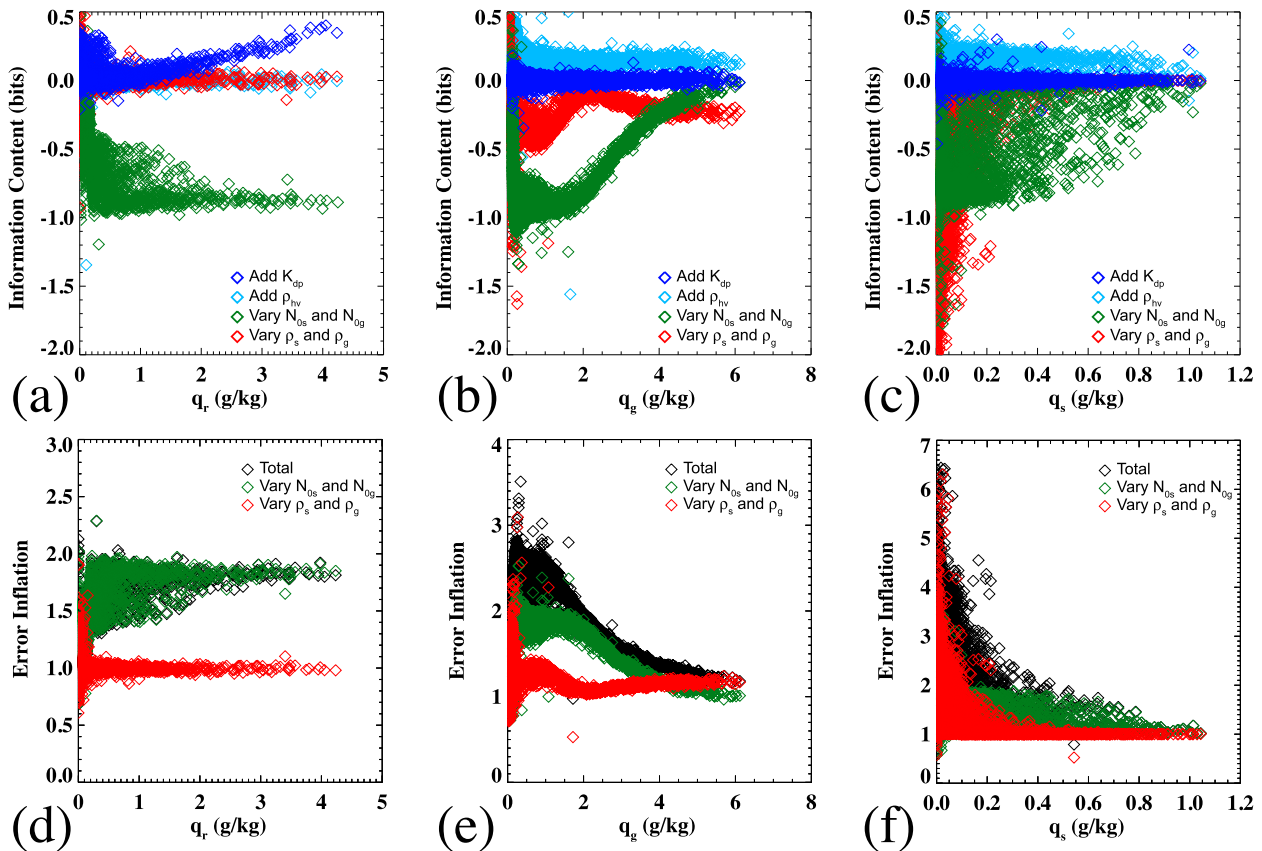


FIG. 10. Results of MCMC experiments using all grid points in the ARMOR domain. Information content gained from addition of K_{dp} and ρ_{hv} observations (blue and cyan, respectively) and lost with variability in N_0 and ice particle density (green and red, respectively) is shown for (a) rain, (b) graupel, and (c) snow. The inflation in the uncertainty of estimated hydrometeors due to variability in N_0 (green), ice particle density (red), and both (black) is shown for (d) rain, (e) graupel, and (f) snow.

snow (up to 650%) than for graupel (up to 350%) and rain (up to 250%).

4. Sensitivity to melting parameterization

As mentioned above, the single-moment microphysical parameterization used in our WRF experiments does not allow for partially melted or partially frozen hydrometeors. In reality, particles that consist of a mixture of liquid and ice exist throughout the region between approximately 0° and -15°C . Since liquid-coated hydrometeors are known to have a strong radar signature, it is useful to examine the effect a melting parameterization may have on the forward model results. To this end, the melting parameterization described above in section 2 is incorporated in the radar forward model. In the process, two new hydrometeor categories are created: one a mixture of rain and graupel, the other a mixture of rain and snow. Each has its own particle size distribution, parameterized via

specified PSD slope intercepts $N_{0,r,s}$ and $N_{0,r,g}$, respectively. As with the control version of the forward model, which does not include melting effects, it is useful to examine the response of radar forward observations to changes in hydrometeor content prior to conducting a Bayesian analysis of the posterior probability distributions. Comparison with response functions for the control model (Fig. 2) reveals subtle changes in structure (Fig. 11). First, we note that melting effectively increases the reflectivity Z_h and Z_v over the entire range of values. This is consistent with the fact that we have chosen a grid point with relatively large values of rain, snow, and graupel. Second, the correlation coefficient values are far lower in the model with melting than in the control version. This is due to the well-known brightband effect on ρ_{hv} . In addition, the response of the correlation coefficient to changes in both rain and graupel is now nonmonotonic. This is due to the fact that we are varying only one hydrometeor content at a time; all others are fixed. For a fixed snow and graupel content, the

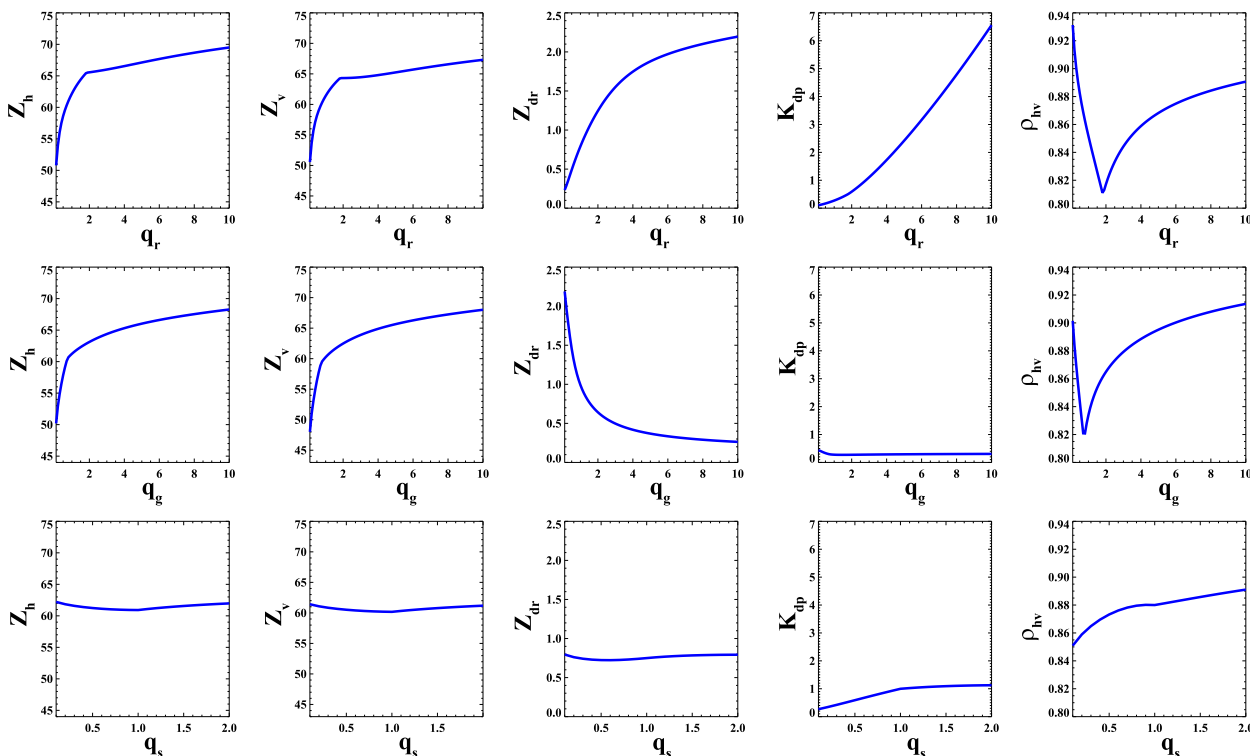


FIG. 11. Response of forward observed radar variables to changes in mixing ratio when a melting parameterization is incorporated in the forward model. (top) q_r vs Z_h , Z_v , Z_{dr} , K_{dp} , and ρ_{hv} . (middle),(bottom) As in (top), but for q_g and q_s vs the same parameters.

reflectivity first increases rapidly as the rain content (and, hence, the mixed-phase fraction) increases. This is because there is both increasing hydrometeor content, and increase in the fraction of liquid-covered ice hydrometeors. Once the rain content exceeds approximately twice the graupel content, the reflectivity signal is primarily derived from the rain content and the contribution to reflectivity from liquid-covered ice hydrometeors is relatively small. As such, the reflectivity response approaches the response seen when the model is run with no melting parameterization (Fig. 2). The nonmonotonic behavior in the correlation coefficient response can be explained similarly. With increasing rain and graupel content (and fixed graupel and rain, respectively), the correlation first decreases as the mixed-phase fraction increases, then increases again as the rain and graupel content become large.

Nonmonotonic response functions are known to give rise to multimode posterior PDFs (Vukicevic and Posselt 2008; Posselt and Vukicevic 2010; Posselt and Bishop 2012; Posselt et al. 2014), and examination of the posterior 1D marginal distributions (Fig. 12) bears this out. Note that the posterior PDFs of rain, snow, and graupel are unimodal when reflectivity, Z_{dr} , and K_{dp} are used as observations, but become distinctly bimodal when ρ_{hv} is included as a constraint. What is notable is the fact

that snow and graupel are much more well constrained (each has a more well-defined mode or modes) when melting is included in the forward model. This is due to the stronger response of reflectivity to changes in snow and graupel content when mixed-phase particles are allowed in the grid box. Reflectivity increases rapidly with hydrometeor content, and as such, there is a much smaller range of hydrometeor mixing ratios that produces reasonable values of forward modeled radar reflectivity.

Additional insight on the effect of melting in the forward model may be obtained from examination of the 2D marginals (Fig. 13). Compared with the results obtained from the forward model without melting (Fig. 7), when melting is turned on, it is clear that the rain mixing ratio is slightly more well constrained, and the snow and hail mixing ratios are much more well constrained. Bimodality is clearly evident in the 2D marginal joint distribution of snow and all of the other parameters, but especially in the joint distribution with rain. The covariances between parameters are left mostly unchanged, due to the fact that the maximum allowed mixed liquid-ice hydrometeor fraction is 50%. This only happens when the rain and graupel content is equal, and generally the mixture in the model grid is very small.

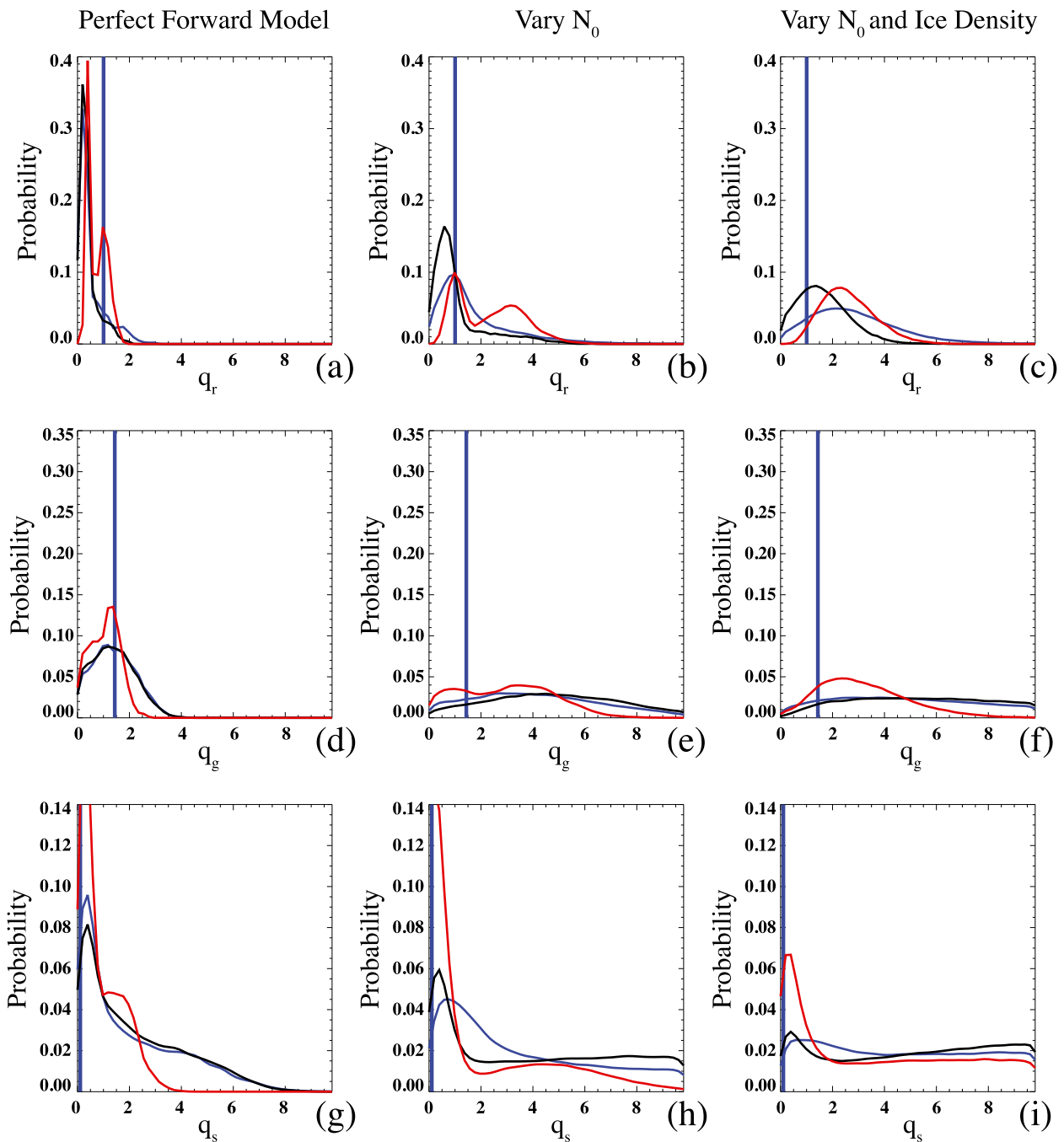


FIG. 12. As in Figs. 5 and 6, but for the case in which the melting parameterization is implemented in the forward model.

5. Summary and conclusions

We have conducted a Bayesian analysis of the information content of dual-pol observations in mixed-phase and ice-only portions of a convective storm, including a detailed examination of individual mixed-phase and ice-only grid points, as well as a sample of more than 9500 ice-containing cloudy grid cells. We

evaluated the influence of a melting parameterization on the results. Our experiments were conducted using an MCMC algorithm that makes no limiting assumptions about the linearity of the forward cloud-radar relationship, and is not restricted to Gaussian probability distributions. As such, it avoids the potentially significant problems associated with estimation of positive definite quantities using least

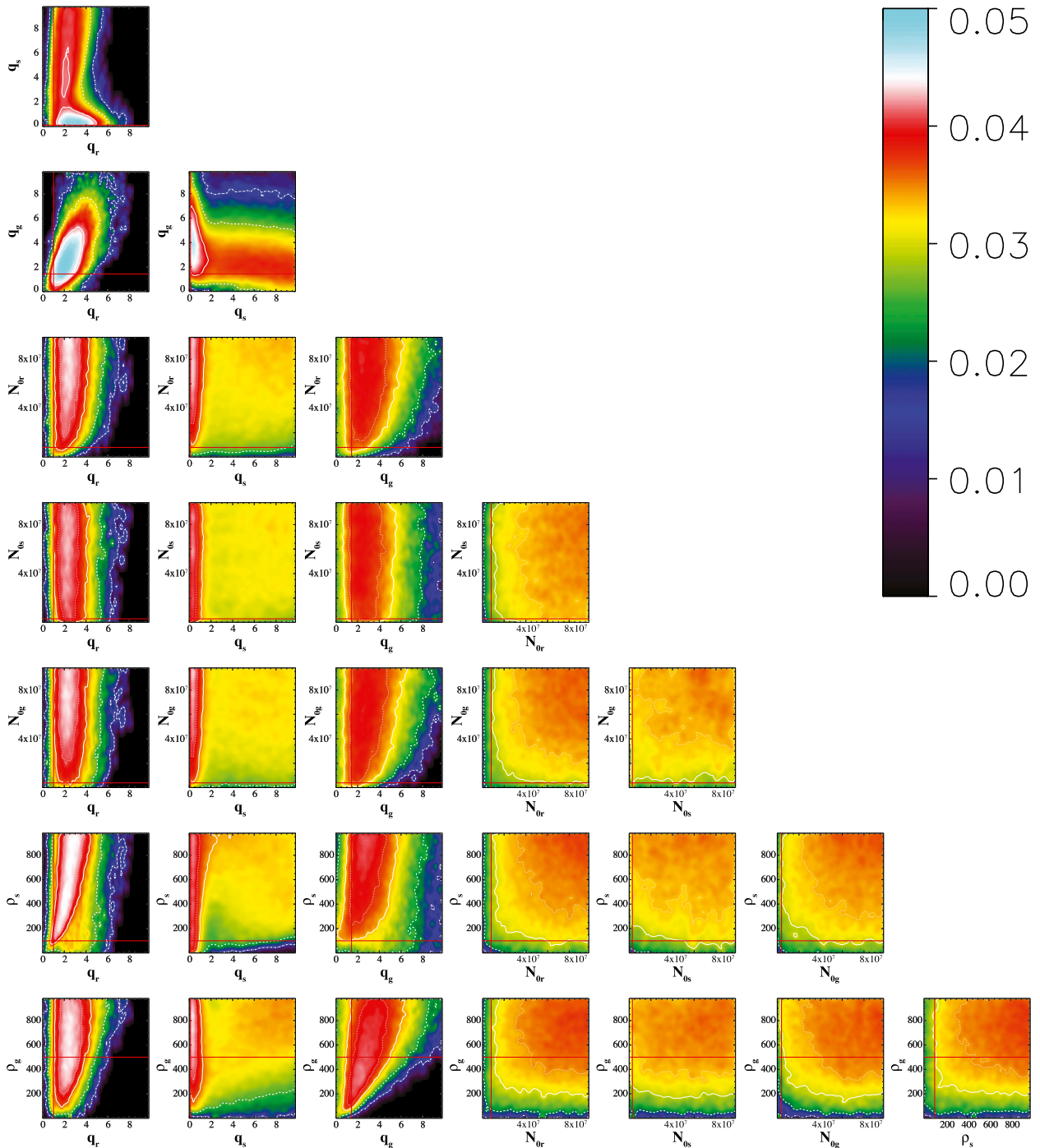


FIG. 13. As in Figs. 7 and 8, but for the case in which the melting parameterization is implemented in the forward model.

squares algorithms, and is not required to return a single unique solution.

The major findings of this work are the following:

- If hydrometeor PSD and ice particle density are assumed known, then dual-pol reflectivity observations (Z_h , Z_v , and Z_{dr}) are sufficient to uniquely

constrain the rain and graupel–hail hydrometeor content. Low-density snow remains poorly constrained, and addition of information in the form of K_{dp} and ρ_{hv} does not produce a unique snow hydrometeor content estimate.

- The fact that hydrometeor content is hard bounded at zero automatically introduces skewness into the

posterior probability distribution for all three hydrometeor types. This will likely cause problems for ensemble data assimilation algorithms based on Gaussian distributions.

- When the intercept of the PSD is allowed to vary, rain content remains relatively well constrained. This is not the case with traditional (nonpolarimetric) radar and as such this represents a significant improvement over older radar systems. In contrast to rain, there is a significant reduction in the information on graupel and snow.
- When ice densities are allowed to vary, the result is a near-complete loss of information on snow content, and a further reduction in the information on graupel–hail.
- An information content analysis indicates that K_{dp} and ρ_{hv} contribute more information to the analysis when a melting parameterization is used.
- Examination of the information loss associated with variability in PSD intercept and ice density indicates errors in the posterior estimate may need to be inflated by up to 400% for rain, 700% for graupel–hail, and 2000% for snow to account for variability in the forward model.

In conclusion, it is important to note the limitations of our study. We have conducted a very thorough analysis of the information contained in dual-polarization radar observations, but our results are limited to a single time during a single case of deep convection. As such, while we are confident we have spanned a large range of hydrometeor contents, we caution against generalizing the results to other convective cases. In addition, very different mixtures of hydrometeors and hydrometeor masses may lead to different information content results. We are currently in the process of analyzing two cases of midlatitude snowfall, but description of this work must, necessarily, be left for the future.

In addition, we have considered only isolated grid cells in our information content analysis. In so doing, we have neglected the fact that reflectivity can (and does) influence the local and far-field thermodynamic state through its influence on the hydrometeor field. In cloudy locations for which the prior contains no cloud, radar assimilation will naturally produce a positive moisture increment (and vice versa for cloud-free regions with cloudy prior). In our experiments, assimilation of radar observations can only have a direct effect on the water vapor content in an already-cloudy grid box. This is because, in our forward models, water vapor and temperature are used only to determine the air density, which is in turn used to obtain the slope of the PSD for the three hydrometeor species. Changes in water vapor

and temperature consistent with the typical uncertainty in these quantities will have a relatively small effect on air density. For example, if we assume an error of 50% on the water vapor content and 2 K on temperature, and consider the 850-hPa pressure level, a temperature of 273 K, and a water vapor mixing ratio of 4 g kg^{-1} , the density perturbation will be less than 1% (0.846%). This translates to a difference in density of 0.0092 kg m^{-3} . The slope of the PSD [Eq. (2)] indicates that a small perturbation in density will have an even smaller effect on the slope due to the fact that the density is raised to a power of $1/4$. We conclude that a change in the air density consistent with typical errors in temperature and water vapor will have a negligible effect on the resulting forward simulated dual-pol variables at any given time in our experiments. We also note that data assimilation that accounts for the time dimension, either by accumulating information from observations sequentially in time (as in the case of ensemble filters) or by dynamically adjusting the model state over some time interval (as in the case of ensemble smoothers or 4DVAR algorithms) may serve to overcome some of the limitations of dual-pol observations we have discussed. In particular, by placing constraint on the rain content early in the storm evolution, the model environment will likely be more realistic, as will the rain hydrometeor content itself. Such improvements should naturally lead to better use of dual-pol information later in the storm life cycle.

It is also important to remind the reader that the results of any information content or data assimilation study are a function of not only the physical system of study, but also the construction of the forward model and forecast model. It is almost certain that use of a different microphysical parameterization (and properly modified radar forward model) would produce different results. We expect this to be true in particular of two- and three-moment parameterizations, for which there is no specified PSD intercept parameter. We also note that there are other well-known sources of uncertainty in the relationship between dual-pol observations and cloud hydrometeor content that are difficult to account for in a gridpoint analysis (e.g., partial beam filling, attenuation, ice crystal shape, etc.).

Finally, we note that, in most retrieval and data assimilation applications, prior information on the state of the system is included in the analysis via use of a prior probability distribution and estimate [the $P(\mathbf{x})$ term in Eqs. (12) and (15)]. In an effort to place an upper bound on the uncertainty in radar forward observations, we have made the assumption that we have no prior information, aside from reasonable bounds on each variable. If, in reality, reliable prior information on the hydrometeor mass, number, or density is available, this

will certainly lead to better posterior constraint on the hydrometeor mass. We take the position that our assumption of no prior information is likely the most realistic, as the capability to provide an accurate prior estimate for cloud mass and PSD does not yet exist in any operational data assimilation system of which we are aware. Even sophisticated multivariate retrieval algorithms struggle mightily to constrain the mass and PSD of ice in both pure ice and mixed-phase clouds (PM14).

Acknowledgments. This work was supported by National Science Foundation Grant AGS-1005354. Marcus van Lier-Walqui and Daniel Hodys provided valuable discussion on the results and conclusions. Two anonymous reviewers provided valuable feedback that helped to clarify and improve the description of the results.

REFERENCES

- Aksoy, A., D. Dowell, and C. Snyder, 2009: A multicaser comparative assessment of the ensemble Kalman filter for assimilation of radar observations. Part I: Storm-scale analyses. *Mon. Wea. Rev.*, **137**, 1805–1824, doi:10.1175/2008MWR2691.1.
- Brandes, E., G. Zhang, and J. Vivekanandan, 2002: Experiments in rainfall estimation with a polarimetric radar in a subtropical environment. *J. Appl. Meteor.*, **41**, 674–685, doi:10.1175/1520-0450(2002)041<0674:EIREWA>2.0.CO;2.
- Bringi, V., V. Chandrasekar, J. Hubbert, E. Gorgucci, W. L. Randeu, and M. Schönhuber, 2003: Raindrop size distribution in different climatic regimes from disdrometer and dual-polarized radar analysis. *J. Atmos. Sci.*, **60**, 354–365, doi:10.1175/1520-0469(2003)060<0354:RSDIDC>2.0.CO;2.
- Carey, L., S. Rutledge, D. Ahijevych, and T. Keenan, 2000: Correcting propagation effects in C-band polarimetric radar observations of tropical convection using differential propagation phase. *J. Appl. Meteor.*, **39**, 1405–1433, doi:10.1175/1520-0450(2000)039<1405:CPEICB>2.0.CO;2.
- Caya, A., J. Sun, and C. Snyder, 2005: A comparison between the 4DVAR and the ensemble Kalman filter techniques for radar data assimilation. *Mon. Wea. Rev.*, **133**, 3081–3094, doi:10.1175/MWR3021.1.
- Chandrasekar, V., V. Bringi, N. Balakrishnan, and D. S. Zrnić, 1990: Error structure of multiparameter radar and surface measurements of rainfall. Part III: Specific differential phase. *J. Atmos. Oceanic Technol.*, **7**, 621–629, doi:10.1175/1520-0426(1990)007<0621:ESOMRA>2.0.CO;2.
- Dowell, C., and L. Wicker, 2009: Additive noise for storm-scale ensemble data assimilation. *J. Atmos. Oceanic Technol.*, **26**, 911–927, doi:10.1175/2008JTECHA1156.1.
- Dudhia, J., 1989: Numerical study of convection observed during the winter monsoon experiment using a mesoscale two-dimensional model. *J. Atmos. Sci.*, **46**, 3077–3107, doi:10.1175/1520-0469(1989)046<3077:NSOCOD>2.0.CO;2.
- Gao, J., M. Xue, K. Brewster, and K. K. Droegemeier, 2004: A three-dimensional variational data analysis method with recursive filter for Doppler radars. *J. Atmos. Oceanic Technol.*, **21**, 457–469, doi:10.1175/1520-0426(2004)021<0457:ATVDAM>2.0.CO;2.
- Haario, H., E. Saksman, and J. Tamminen, 1999: Adaptive proposal distribution for random walk Metropolis algorithm. *Comput. Stat.*, **14**, 375–395, doi:10.1007/s001800050022.
- Hall, M., J. Goddard, and S. Cherry, 1984: Identification of hydrometeors and other targets by dual-polarization radar. *Radiol. Sci.*, **19**, 132–140, doi:10.1029/RS019i001p00132.
- Heymsfield, A. J., A. Bansemer, P. R. Field, S. L. Durden, J. L. Smith, J. E. Dye, W. Hall, and C. A. Grainger, 2002: Observations and parameterizations of particle size distributions in deep tropical cirrus and stratiform precipitating clouds: Results from in situ observations in TRMM field campaigns. *J. Atmos. Sci.*, **59**, 3457–3491, doi:10.1175/1520-0469(2002)059<3457:OAIPOPS>2.0.CO;2.
- Hong, S.-Y., Y. Noh, and J. Dudhia, 2006: A new vertical diffusion package with an explicit treatment of entrainment processes. *Mon. Wea. Rev.*, **134**, 2318–2341, doi:10.1175/MWR3199.1.
- , K. S. Sunny Lim, J. H. Kim, J. O. Jade Lim, and J. Dudhia, 2009: Sensitivity study of cloud-resolving convective simulations with WRF using two bulk microphysical parameterizations: Ice-phase microphysics versus sedimentation effects. *J. Appl. Meteor. Climatol.*, **48**, 61–76, doi:10.1175/2008JAMC1960.1.
- Hu, M., M. Xue, J. Gao, and K. Brewster, 2006: 3DVAR and cloud analysis with WSR-88D level-II data for the prediction of Fort Worth tornadic thunderstorms. Part II: Impact of radial velocity analysis via 3DVAR. *Mon. Wea. Rev.*, **134**, 699–721, doi:10.1175/MWR3093.1.
- Jung, Y., M. Xue, G. Zhang, and J. M. Straka, 2008a: Assimilation of simulated polarimetric radar data for a convective storm using the ensemble Kalman filter. Part I: Observation operators for reflectivity and polarimetric variables. *Mon. Wea. Rev.*, **136**, 2228–2245, doi:10.1175/2007MWR2083.1.
- , —, —, and —, 2008b: Assimilation of simulated polarimetric radar data for a convective storm using the ensemble Kalman filter. Part II: Impact of polarimetric data on storm analysis. *Mon. Wea. Rev.*, **136**, 2246–2260, doi:10.1175/2007MWR2288.1.
- , —, —, and —, 2010: Simulations of polarimetric radar signatures of a supercell storm using a two-moment bulk microphysics scheme. *J. Appl. Meteor. Climatol.*, **49**, 146–163, doi:10.1175/2009JAMC2178.1.
- Kawabata, T., T. Kuroda, H. Seko, and K. Saito, 2011: A cloud-resolving 4DVAR assimilation experiment for a local heavy rainfall event in the Tokyo metropolitan area. *Mon. Wea. Rev.*, **139**, 1911–1931, doi:10.1175/2011MWR3428.1.
- Kumjian, M. R., 2013: Principles and applications of dual-polarization weather radar. Part I: Description of the polarimetric radar variables. *J. Oper. Meteor.*, **1**, 226–242, doi:10.1519/nwajom.2013.0119.
- Li, X., and J. Mecikalski, 2010: Assimilation of the dual-polarization Doppler radar data for a convective storm with a warm-rain radar forward operator. *J. Geophys. Res.*, **115**, D16208, doi:10.1029/2009JD013666.
- , and —, 2012: Impact of the dual-polarization Doppler radar data on two convective storms with a warm-rain radar forward operator. *Mon. Wea. Rev.*, **140**, 2147–2167, doi:10.1175/MWR-D-11-00090.1.
- , and —, 2013: Evaluation of the sensitivity of the dual-polarization Doppler radar data assimilation to radar forward operator. *J. Meteor. Soc. Japan*, **91**, 287–304, doi:10.2151/jmsj.2013-304.
- Mlawer, E., S. Taubman, P. Brown, M. Iacono, and S. Clough, 1997: Radiative transfer for inhomogeneous atmosphere: RRTM, a validated correlated-k model for the longwave. *J. Geophys. Res.*, **102**, 16 663–16 682, doi:10.1029/97JD00237.

- Posselt, D. J., 2013: Markov chain Monte Carlo methods: Theory and applications. *Data Assimilation for Atmospheric, Oceanic and Hydrologic Applications*, 2nd ed. S. K. Park and L. Xu, Eds., Springer, 59–87.
- , and T. Vukicevic, 2010: Robust characterization of model physics uncertainty for simulations of deep moist convection. *Mon. Wea. Rev.*, **138**, 1513–1535, doi:10.1175/2009MWR3094.1
- , and C. H. Bishop, 2012: Nonlinear parameter estimation: Comparison of an ensemble Kalman smoother with a Markov chain Monte Carlo algorithm. *Mon. Wea. Rev.*, **140**, 1957–1974, doi:10.1175/MWR-D-11-00242.1
- , and G. G. Mace, 2014: MCMC-based assessment of the error characteristics of a combined radar-passive microwave cloud property retrieval. *J. Appl. Meteor. Climatol.*, **53**, 2034–2057, doi:10.1175/JAMC-D-13-0237.1
- , T. S. L'Ecuyer, and G. L. Stephens, 2008: Exploring the error characteristics of thin ice cloud property retrievals using a Markov chain Monte Carlo algorithm. *J. Geophys. Res.*, **113**, D24206, doi:10.1029/2008JD010832
- , D. Hodyss, and C. H. Bishop, 2014: Errors in ensemble Kalman smoother estimates of cloud microphysical parameters. *Mon. Wea. Rev.*, **142**, 1631–1654, doi:10.1175/MWR-D-13-00290.1
- Rabier, F., H. Järvinen, E. Klinker, J.-F. Mahfouf, and A. Simmons, 2000: The ECMWF operational implementation of four-dimensional variational assimilation. I: Experimental results with simplified physics. *Quart. J. Roy. Meteor. Soc.*, **126**, 1143–1170, doi:10.1002/qj.49712656415
- Rinehart, R. E., 1997: *Radar for Meteorologists*. Rinehart Publications, 428 pp.
- Rodgers, C. D., 2000: *Inverse Methods for Atmospheric Sounding: Theory and Practice*. World Scientific, 240 pp.
- Roy, S. S., R. K. Datta, R. C. Bhatia, and A. K. Sharma, 2005: Drop size distributions of tropical rain over south India. *Geofizika*, **22**, 105–130.
- Ryzhkov, A., D. Zrnić, and B. Gordon, 1998: Polarimetric method for ice water content determination. *J. Appl. Meteor.*, **37**, 125–134, doi:10.1175/1520-0450(1998)037<0125:PMFIWC>2.0.CO;2
- Sachidananda, M., and D. S. Zrnić, 1987: Rain rate estimates from differential polarization measurements. *J. Atmos. Oceanic Technol.*, **4**, 588–598, doi:10.1175/1520-0426(1987)004<0588:RRFDP>2.0.CO;2
- Schenkman, A., M. Xue, A. Shapiro, K. Brewster, and J. Gao, 2011: Impact of CASA radar and Oklahoma mesonet data assimilation on the analysis and prediction of tornadic mesovortices in a MCS. *Mon. Wea. Rev.*, **139**, 3422–3445, doi:10.1175/MWR-D-10-05051.1
- Seliga, T., and V. Bringi, 1976: Potential use of radar differential reflectivity measurements at orthogonal polarizations for measuring precipitation. *J. Appl. Meteor.*, **15**, 69–76, doi:10.1175/1520-0450(1976)015<0069:PUORDR>2.0.CO;2
- Skamarock, W. C., and Coauthors, 2008: A description of the Advanced Research WRF version 3. NCAR Tech. Note NCAR/TN-475+STR, 113 pp. [Available online at http://www.mmm.ucar.edu/wrf/users/docs/arw_v3_bw.pdf.]
- Straka, J., D. Zrnić, and A. Ryzhkov, 2000: Bulk hydrometeor classification and quantification using polarimetric radar data: Synthesis of relations. *J. Appl. Meteor.*, **39**, 1341–1372, doi:10.1175/1520-0450(2000)039<1341:BHCAQU>2.0.CO;2
- Sun, J., 2005: Initialization and numerical forecasting of a supercell storm observed during STEPS. *Mon. Wea. Rev.*, **133**, 793–813, doi:10.1175/MWR2887.1
- , and N. Crook, 1997: Dynamical and microphysical retrieval from Doppler radar observations using a cloud model and its adjoint. Part I: Model development and simulated data experiments. *J. Atmos. Sci.*, **54**, 1642–1661, doi:10.1175/1520-0469(1997)054<1642:DAMRFD>2.0.CO;2
- , and —, 1998: Dynamical and microphysical retrieval from Doppler radar observations using a cloud model and its adjoint. Part II: Retrieval experiments of an observed Florida convective storm. *J. Atmos. Sci.*, **55**, 835–852, doi:10.1175/1520-0469(1998)055<0835:DAMRFD>2.0.CO;2
- Tamminen, J., and E. Kyrölä, 2001: Bayesian solution for nonlinear and non-Gaussian inverse problems by Markov chain Monte Carlo method. *J. Geophys. Res.*, **106**, 14377–14390, doi:10.1029/2001JD900007
- Tokay, A., and D. A. Short, 1996: Evidence from tropical rain-drop spectra of the origin of rain from stratiform versus convective clouds. *J. Appl. Meteor.*, **35**, 355–371, doi:10.1175/1520-0450(1996)035<0355:EFTRSO>2.0.CO;2
- Tong, M., and M. Xue, 2008: Simultaneous estimation of microphysical parameters and atmospheric state with simulated radar data and ensemble square root Kalman filter. Part I: Sensitivity analysis and parameter identifiability. *Mon. Wea. Rev.*, **136**, 1630–1648, doi:10.1175/2007MWR2070.1
- Vivekanandan, J., S. Ellis, R. Oye, D. Zrnić, A. Ryzhkov, and J. Straka, 1999: Cloud microphysics retrieval using S-band dual-polarization radar measurements. *Bull. Amer. Meteor. Soc.*, **80**, 381–388, doi:10.1175/1520-0477(1999)080<0381:CMRUSB>2.0.CO;2
- , G. Zhang, and E. Brandes, 2004: Polarimetric radar estimators based on a constrained gamma drop size distribution model. *J. Appl. Meteor.*, **43**, 217–230, doi:10.1175/1520-0450(2004)043<0217:PREBOA>2.0.CO;2
- Vukicevic, T., and D. Posselt, 2008: Analysis of the impact of model nonlinearities in inverse problem solving. *J. Atmos. Sci.*, **65**, 2803–2823, doi:10.1175/2008JAS2534.1
- Wang, H., J. Sun, S. Fan, and X.-Y. Huang, 2013: Indirect assimilation of radar reflectivity with WRF 3D-Var and its impact on prediction of four summertime convective events. *J. Appl. Meteor. Climatol.*, **52**, 889–902, doi:10.1175/JAMC-D-12-0120.1
- Wattrelot, E., O. Caumont, and J.-F. Mahfouf, 2014: Operational implementation of the 1D+3D-Var assimilation method of radar reflectivity data in the AROME model. *Mon. Wea. Rev.*, **142**, 1852–1873, doi:10.1175/MWR-D-13-00230.1
- Xiao, Q., Y.-H. Guo, J. Sun, W.-C. Lee, D. M. Barker, and E. Lim, 2007: An approach of radar reflectivity data assimilation and its assessment with the inland QPF of Typhoon Rusa (2002) at landfall. *J. Appl. Meteor. Climatol.*, **46**, 14–22, doi:10.1175/JAM2439.1
- Zhang, F., Y. Weng, J. Sippel, Z. Meng, and C. Bishop, 2009: Cloud-resolving hurricane initialization and prediction through assimilation of Doppler radar observations with an ensemble Kalman filter. *Mon. Wea. Rev.*, **137**, 2105–2125, doi:10.1175/2009MWR2645.1
- Zhang, G., J. Vivekanandan, and E. Brandes, 2001: A method for estimating rain rate and drop size distribution from polarimetric radar measurements. *IEEE Trans. Geosci. Remote Sens.*, **39**, 830–841, doi:10.1109/36.917906
- Zrnić, D., and A. Ryzhkov, 1996: Advantages of rain measurements using specific differential phase. *J. Atmos. Oceanic Technol.*, **13**, 454–464, doi:10.1175/1520-0426(1996)013<0454:AORMUS>2.0.CO;2